The Dissertation Committee for Benjamin Ashley Huntington Certifies that this is the approved version of the following dissertation:

Interfacial Dynamics in Processing of Materials with Normal Stress Differences

Committee:

Roger T. Bonnecaze, Supervisor

Benny D. Freeman

Venkat Ganesan

Kamy Sepehrnoori

Interfacial Dynamics in Processing of Materials with Normal Stress Differences

by

Benjamin Ashley Huntington

Dissertation

Presented to the Faculty of the Graduate School of

The University of Texas at Austin

in Partial Fulfillment

of the Requirements

for the Degree of

Doctor of Philosophy

The University of Texas at Austin

December 2017

Dedication

Dedicated to my supportive parents, John and Sharon Huntington, and my brother Phillip Huntington who were always there to encourage me.

Acknowledgements

I would first like to thank my advisor Dr. Roger Bonnecaze. He has been not only a good academic advisor, but also a caring mentor. He found time to meet with me nearly every week, despite his increasingly busy schedule. He helped me find projects that I would enjoy working on and find interesting and valuable. He has also helped me to expand my career options by encouraging me to take an internship at Exxon Mobil and has given me valuable career advice and lessons that I will take with me to my postdoc.

I would also like to thank Dr. Joao Maia and his lab group, in particular Patrick Harris, Rongzhi Huang, Sid Carson, Ricardo Andrade, and Jessica Patz for the great experiments that they did that added so much understanding and validation for my simulations. They were always available to answer any question that I had about the co-extruder and the experiments and taught me a lot about the co-extrusion process. They were very kind to make sure that any trip I made to Case Western Reserve University was pleasant and productive.

I would also like to thank Dr. Cloitre for the roll-to-roll experiments he performed on soft particle pastes. The photos, video, and data from these experiments have been very helpful for the work I have done in my dissertation.

I really enjoyed my time working in the Bonnecaze group. I would like to thank my labmates Soumik Das, Akhilesh Jain, Lavanya Mohan, Tian Fei Liu, Mohammad Shafiei, Shruti Jain, Meghali Chopra, Mark Ferraro, Talha Arshad, Mike Clements, Parag Katira, Andrew Spann, Fardin Khabaz, Xilan Zhu, Steven Stanley, and Yang Ban for the lunches and chats.

Finally, I would like to thank my parents, John and Sharon Huntington, my brother Phillip Huntington, and my girlfriend Sasha Miao for their constant love and support.

Interfacial Dynamics in Processing of Materials with Normal Stress Differences

Benjamin Ashley Huntington, Ph.D.
The University of Texas at Austin, 2017

Supervisor: Roger T. Bonnecaze

Processing of elastic non-Newtonian fluids is of critical importance to many industrial manufacturing processes. Three different processes are analyzed in this work: co-extrusion of polymer melts, inclined plane flow of soft particle pastes, and roll-to-roll processing of soft particle pastes. These three processes are examined using stability theory and finite element simulation as tools and, when possible, experimental results obtained by collaborators are used to verify and test findings.

The polymer co-extrusion process analyzed in this work is an experimental device at Case Western Reserve University (CWRU) that creates many layered polymer films with individual layer thicknesses on the order of microns to 100s of nanometers. Due to forces acting between the layers during the co-extrusion process, the layered structure can be damaged or destroyed. Two key components of this process are analyzed using the finite element method: the feedblock for the co-extruder and the layer multiplier dies. The study of the feedblock identifies two critical improvements for the process that help mitigate the destruction of the layered structure. The finite element analysis of the multiplier dies identify a way to reduce the high pressure drop through the multiplier die, and a design that

helps preserve the layered structure. These results are confirmed experimentally by collaborators at CWRU.

In the second part of this work, flow of a soft particle paste down an inclined plane is analyzed using a linear stability theory. This problem is tackled a preliminary study to the roll-to-roll processing of the same material. Stability of inclined plane flow has been studied in the literature for a variety of different materials. The destabilizing second normal stress differences exhibited by the soft particle paste are found to compete with the stabilizing force of surface tension. Stable and unstable wavenumber ranges are determined for this problem, as well as the fastest growing mode. This is then used to compute the expected wave lengths seen for varying yield stress.

Lastly, the stability of flow of a soft particle paste in a forward roll coating process is analyzed. Forward roll coating of soft particle pastes is a common industrial process, particularly in the area of paint application. The analysis examines the impact of material properties on the so –called ribbing instability that is known to occur in many roll-to-roll processes. A method for analyzing the stability of Newtonian fluids in forward roll coating is expanded to power law fluids. The results show that stability strongly depends on the capillary number and the power law index.

Table of Contents

List of Tables

List of Figures

Chapter 1: Introduction

1.1 Why Study Processing of Elastic Fluids?

Fluid shaping and coating processes are vital to many manufacturing processes in the chemical coating and polymer industries. Some examples of fluid shaping processes include blow molding [Schroers et al. (2007); Lee N.C. (2000)] which is used to manufacture glass and plastic bottles, injection molding [Rosato and Rostato (2012); German (1990)] which is used to manufacture solid plastic components and products in batches, and extrusion/co-extrusion [Michaeli (2003); Denn (2008)], which is used to continuously form products such as pipe by pushing molten material through a shaped die. Some examples of commonly used coating techniques are slot die coating [Krebs et al. (2009); Allstrup, J et al. (2010)] and roll-to-roll coating [Coyle et al. (1986); Carvalho et al. (1999)]. The two processes that are of most interest are co-extrusion and roll-to-roll coating of a substrate. Both of these processes can be disrupted by interfacial deformation and can be improved by understanding the nature of this deformation.

Co-extrusion is a process by which multiple materials are driven through a die together to create a product that takes advantage of the combination of material properties and the structure that is generated. One example of this is co-extruded medical tubing for insulin delivery, which is shown in Fig. 1.1. The specific co-extrusion process addressed in this work creates layered structures with hundreds to thousands of layers made of different polymers with thicknesses in the range of microns to hundreds of nanometers [Ponting et al. (2010)]; This method of co-extrusion is capable of producing materials with

a wide range of novel functions. Applications for these materials include water purifying membranes [Geise et al. (2010)], gas separation membranes [Armstrong et al. (2014)], lenses with tunable refractive indices [Ji et al. (2013)], and optical data storage [Lott et al. (2011); Ryan et al. (2012)].

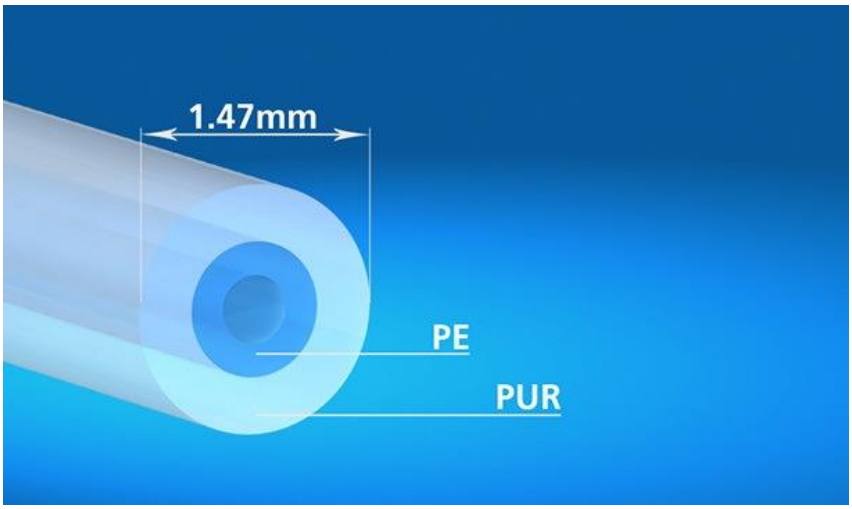

Figure 1.1: Co-extruded tubing for insulin delivery. The inside of the tube is made with polyethylene which does not absorb insulin, allowing more insulin to reach the body. The outer side of the tube is made with polyurethane which is tough and flexible so as to protect the inner tube. Image taken from https://www.raumedic.com/technologies/extrusion/co-extrusion/.

Roll-to-roll coating is the second type of fluid processing that will be analyzed in this work. Roll-to-roll coating is a method for spreading fluid onto a substrate in a continuous fashion. The roll-to-roll coating process is characterized by two cylinders that are coated in fluid, situated close to each other, and rotating about their central axis. Fig 1.2 shows a picture of a roll-to-roll process for coating steel and aluminum coil. The two rollers rotating together help to ensure that a flat and even coating of the fluid is applied to

the surface of one or both of the rollers. Roll-to-roll coating has been thoroughly examined in the literature for Newtonian fluids [Pitts and Greiller (1961); Savage (1984, 1977, 1977); Greener et al. (1980)]. This work is focused in particular on the coating of visco-plastic fluids, where significantly less is known about them. Roll coating of visco-plastic fluids is used in paint application [Cohu and Magnin (1995); Lopez and Rosen (2002)] and coating of photo-voltaics [Krebs (2009, 2009)].

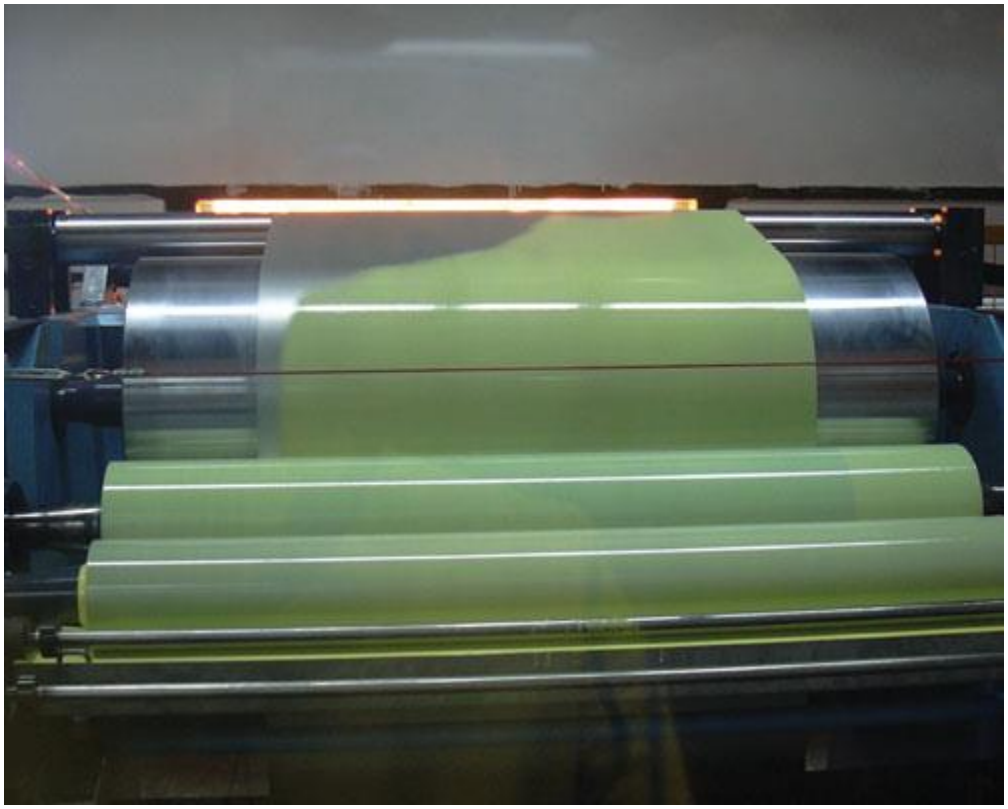

Figure 1.2: A roll-to-roll coating machine is shown. This machine is used to apply paint to aluminum and steel coils. This image is taken from the website of the company that produces the machine, http://www.ttnet.net/ttnet/gotoprd/MN560/050/0/2513030343731383 73.htm .

This work covers four major projects:

- Re-design of the Co-extrusion Feedblock
- Re-design of the Co-extrusion Multiplier Die
- Stability Analysis of Inclined Plane Flow of a Soft Particle Paste
- Stability Analysis of Roll-to-Roll Coating of Soft Particle Paste

These projects are introduced in the following sections and then will be covered in detail in each chapter.

1.2 Multi-layer Co-extrusion

The co-extrusion process that is the focus of this work is one that generates many layered polymer films with layer numbers in the 100s up to 1000 layers with thicknesses on the order of microns to 100s of nanometers. The experimental co-extruder device resides at Case-Western Reserve University in Cleveland, Ohio. Many of the computational results presented in this work were tested by experimental collaborators on this device.

The co-extrusion process begins as two or three polymers are melted and pushed by separate extruders into a feedblock where the different materials meet to form a two or three layer rectangular block. This rectangular block is then fed into a series of multiplier dies which split the stacked flow that they receive in half and then stack the two flows on top of each other to effectively double the number of layers in the flow. Fig. 1.3 shows a diagram of this process as a whole. Fig. 1.4 shows a picture of the actual co-extruder used by our experimental collaborators. Fig. 1.5 shows a 3-D drawing of a multiplier die.

Many applications for these layered materials require flat interfaces between the different polymer layers. During the co-extrusion process, however, forces between the

different fluid layers result in interface deformation between the fluids. In some cases, deformation is so severe that surrounding layers completely encapsulate a middle layer, destroying the desired layered structure. Fig. 1.6 shows a cross-section of a four-layer flow with a complete encapsulation of one of the layers.

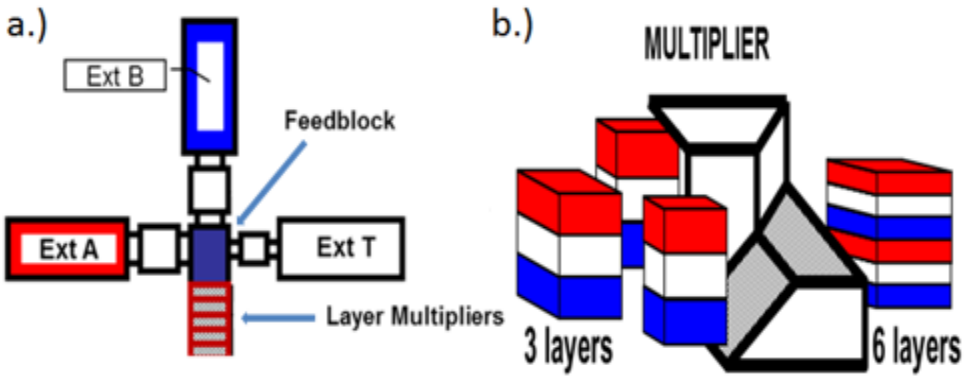

Figure 1.3: a.) Diagram of the multi-layering co-extruder. Up to three polymers enter the feedblock and then flow through the multiplier dies. The final product is a material with a multi-layered cross-section. b.) diagram of how a three layer flow is split and then stacked to create a six layer flow in a multiplier die.

Figure 1.4: Graduate students operating the co-extruder at Case Western Reserve University. A thin film is seen being extruded as a student pulls the film out.

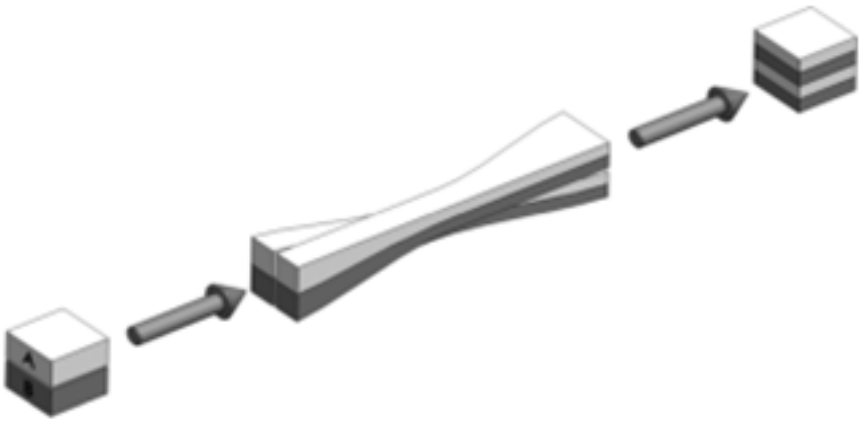

Figure 1.5: A multiplier design is shown with a two layer structure made up of two fluids entering, A and B, and a 4 layer structure exits. The two layer flow is split into two different flows, one on the left and one on the right. The left two layer flow is pushed downward and the right side flow is pushed upwards and then the flows are stacked on top of each other to make a four layer flow at the exit.

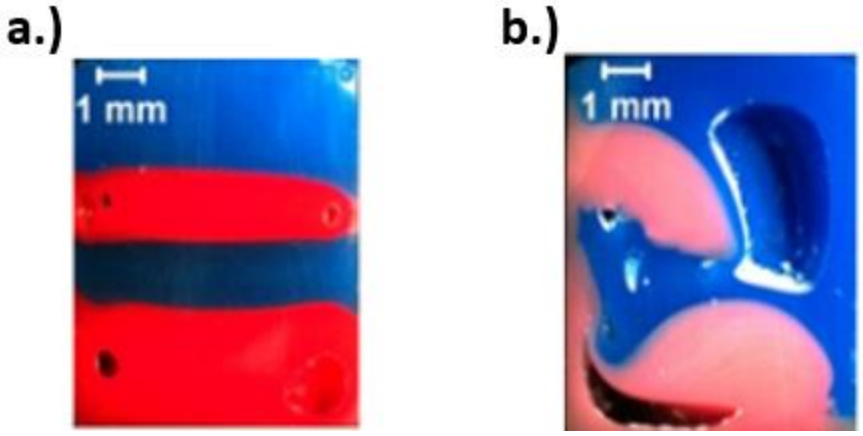

Figure 1.6: Photos of experimental cross-sections of two different polymer pairs with four layers each taken by collaborators at Case Western Reserve University. (a) Co-extrusion of PMMA VS 100 (red) with polystyrene(PS) (blue) and (b) shows a pairing of PMMA VS 826 (pink) with PS (blue). In (a), flat even layers are generated by the co-extrusion while in (b) the blue fluid has completely encapsulated the pink layer near the top. This leads to substantial deformation of the fluid interfaces and a total destruction of the layered structure in (b).

This work seeks to address the problem of interfacial deformation between different polymer layers. The problem is tackled in two parts. The first part examines how design and process changes can be implemented in the feedblock to mitigate interface deformation there. This is very important because interface deformation in the feedblock is propagated throughout all of the multiplier dies, so minimizing deformation in the feedblock is essential. The second part seeks to redesign the multiplier dies. The first of these new

designs aims to reduce the pressure drop required to push the flow through the die. The second looks at how the multiplier die design can be changed to reduce interface deformation in the final layered product.

1.3 Stability of Visco-Plastic Flows in Processing

The stability analysis of a forward roll-to-roll coating process and the stability of for visco-plastic fluids makes up the second part of this work. First, the problem of stability of a visco-plastic flow down an inclined plane is studied. This part examines the effects of a non-zero second normal stress difference on the stability of flow of visco-plastic flows. The visco-plastic materials referred to here are specifically those that have a shear stress relationship given by the Herschel-Bulkley constitutive relationship and a non-zero second normal stress difference that is a function of shear rate. The second normal stress difference is defined as $N_2 = \sigma_{22} - \sigma_{33}$, where N_2 is the second normal stress difference, σ_{22} and σ_{33} are the normal stress components perpendicular to the direction of flow. A figure showing the expected flow profile and interface perturbation is shown in Fig. 1.7.

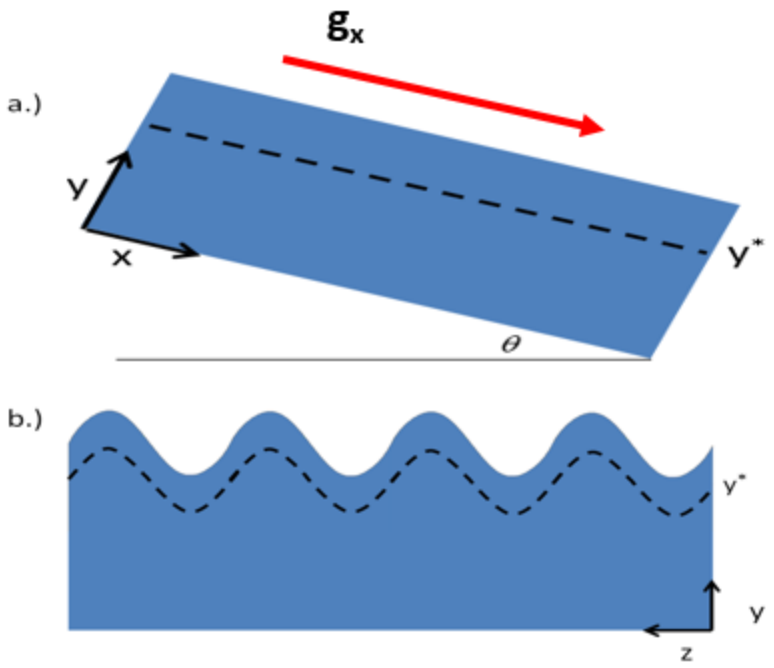

Figure 1.7: Diagram of flow problem for a visco-plastic fluid flowing down an inclined plane due to gravity. (a) shows the direction of gravitational acceleration parallel to the inclined plane's surface. (b) shows the transverse direction where the perturbation is to be applied. The disturbance is applied in the transverse direction because that is the plane that elastic forces are acting in. the dashed line labeled y^* is a line above which the material is solid.

Flow down an inclined plane of a visco-plastic fluid with a second normal stress difference is characterized by a balance between gravitational acceleration and shear force at the inclined surface. The second normal stress difference that results from this shear is explored as a means of destabilizing the flow to disturbances perpendicular to it, as seen in Fig. 1.7 (b). The steady state and perturbed velocity profiles are solved for. Then the standard linear stability analysis technique is applied to determine ranges of stable and unstable wave numbers and the fastest growing unstable wave mode.

The second part of this work seeks to determine the stability conditions required for operating a forward roll-to-roll coating process using a visco-plastic fluid. A diagram of the system is shown in Fig. 1.8. This stability analysis looks at the interface between the liquid and the air to investigate the so-called "ribbing" instability [Pitts and Greiller (1961)]. The ribbing instability in roll-to-roll coating is characterized by periodic thickness striations in the coating liquid along the axis of the rotating cylinders. A picture of an experimental roll-to-roll set-up demonstrating this instability is seen in Fig. 1.9. The purpose of this part of the work is to understand which processing parameters control stability and look for where flow is stable and unstable. To do this, the method of analysis employed by [Savage (1984)] is modified to be used on visco-plastic fluids. This method provides curves showing where stable and unstable operating conditions reside.

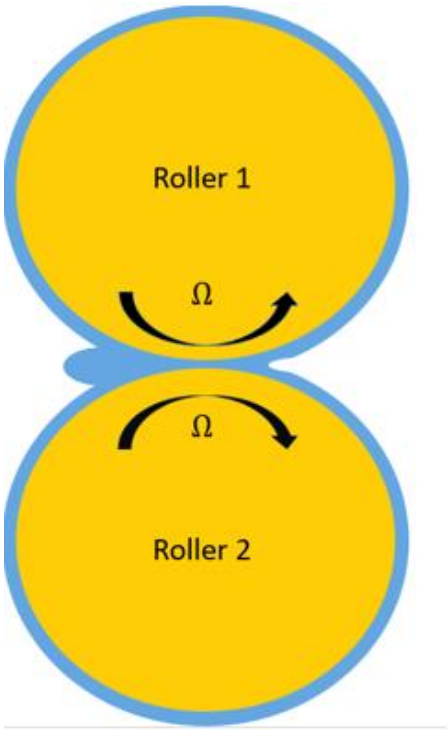

Figure 1.8 2-D diagram of a roll-to-roll coating process where fluid is shown in blue and rollers are shown in yellow, rotating with rotational speed Ω. A fluid bank is built up on the left where the flows converge and a meniscus forms on the right where the flows diverge. This meniscus is where the instability is studied.

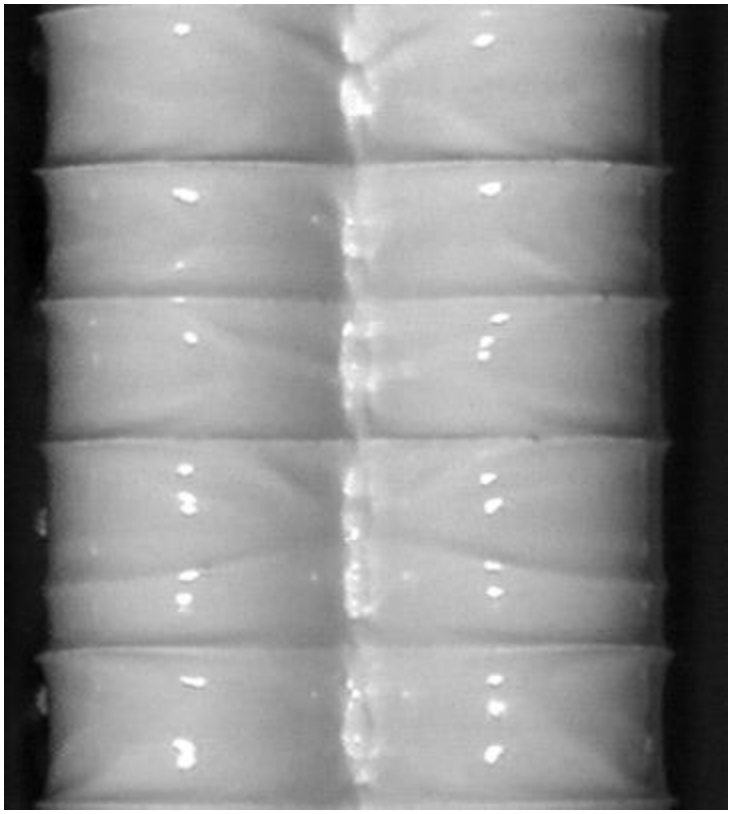

Figure 1.9 Photo of flow of a paste in a forward roll-to-roll set-up. The flow in the center is going into the page and the excess material is seen bulging out in the gap, as is illustrated in Fig. 1.8. Multiple thickness striations (ribs) are seen horizontally across both rollers. Experiment performed in Dr. Michel Cloitre's lab.

Chapter 2: Simulation of Multi-layered Polymer Flow in a Feedblock

2.1 Introduction

Some parts of this chapter is taken from [Huntington, B.A., et al. (2013)]. Co-extrusion is a process by which layered polymer products can be continuously formed [Mueller et al. (1997); Schrenk et al. (1996); Han (1976); Jarus et al. (2002)]. This process is advantageous because it can create finely layered structures cheaply and continuously. Of particular interest are many layered polymer structures with very fine layers with thicknesses on the order of micron[1]s to hundreds of nanometers. These materials can be used in a variety of different applications including water purifying membranes [Geise et al. (2010)], gas separation membranes [Armstrong et al. (2014)], lenses with tunable refractive indices [Ji et al. (2013)], and optical data storage [Lott et al. (2011); Ryan et al. (2012)]. This process works by feeding layered polymer fluids into a series of multiplier dies which split and stack the layered structure to double the number of layers in each multiplier die.

The co-extrusion process begins by co-extruding materials through the feedblock. The feedblock is a simple die of rectangular cross-section which serves to guide the layered structure into the subsequent multiplier dies (see Fig. 1.4). Controlling interface distortion in the feed block is clearly vital to the success of the co-extrusion process because the interface distortions that occur here are propagated later on in the multiplier dies. It is,

[1] Material in this chapter published in: Huntington, B. A. et al. (2013). Distortion of Interfaces in a Multilayer Polymer Co-extrusion Feedblock. *International Polymer Processing*, *28*(3), 274-280. I contributed by writing the paper and doing all the simulations.

therefore, important to understand the factors that influence these distortions and make process changes to mitigate them.

The topic of interface deformation in polymer co-extrusion is of considerable interest and has been studied thoroughly [Debbaut et al. (1997); Dooley (2002); Gifford (1997, 2000); Karagiannis et al. (1990); Sunwoo et al. (2001); White and Lee (1997); Wilson and Khomami (1992, 1993); Borzachiello et al. (2014); Yue et al. (2008); Perdikoulias, J. et al. (1995)]. In this chapter, simulations are used to understand the effects of rheology on the distortion of the interfaces in the feedblock and to explore two different methods of improving layer flatness and uniformity in the feedblock. Simulations are first performed for two and three layer flows of two different pairs of materials and the results are experimentally validated by our collaborators at Case Western Reserve University. The first method investigated for mitigating interface deformation is to increase the number of layers in the feedblock. The second method is to decrease the friction at the walls. Both of these methods seek to modify the second normal stress differences present in the channel as they are responsible for deformation of the interfaces.

2.2 Simulation Method

Multi-layered flow in a rectangular feedblock as shown in Fig. 2.1 is considered. Two or more layers of two types of immiscible viscoelastic polymers are injected at the entrance of the channel and we wish to determine the evolution of the shapes of the interfaces as the flow progresses down the feedblock by solving the equations for the conservation of mass and momentum given by:

$$\nabla \cdot \mathbf{u} = 0 \ , \tag{2.1}$$

$$\nabla \cdot \mathbf{T} - \nabla p = 0 \ , \tag{2.2}$$

where **u** is the velocity, **T** is the stress, and p is the pressure. The rheology of the polymers is described by the Phan-Thien Tanner (PTT) constitutive model [Larson (1999)], which is given by:

$$\mathbf{T} = \mathbf{T}_1 + \mathbf{T}_2 \ , \tag{2.3}$$

$$\mathbf{T}_2 = 2\eta_2 \mathbf{D} \ , \tag{2.4}$$

$$\exp\left(\frac{\varepsilon\lambda}{\eta_1}\mathrm{tr}(\mathbf{T}_1)\right)\mathbf{T}_1 + \lambda\left(\left(1-\frac{\xi}{2}\right)\overset{\nabla}{\mathbf{T}}1 + \frac{\xi}{2}\overset{\Delta}{\mathbf{T}}1\right) = 2\eta_1\mathbf{D}, \tag{2.5}$$

$$\overset{\nabla}{\mathbf{T}}_1 = \mathbf{u}\cdot\nabla\mathbf{T}_1 - \left(\nabla\mathbf{u}\right)^{\mathrm{T}}\cdot\mathbf{T}_1 - \mathbf{T}_1\cdot\left(\nabla\mathbf{u}\right) \ , \tag{2.6}$$

$$\overset{\Delta}{\mathbf{T}}1 = \mathbf{u}\cdot\nabla\mathbf{T}_1 + \left(\nabla\mathbf{u}\right)^{\mathrm{T}}\cdot\mathbf{T}_1 + \mathbf{T}_1\cdot\left(\nabla\mathbf{u}\right) \tag{2.7}$$

where $\mathbf{T_1}$ is the elastic component of the stress $\mathbf{T_2}$ is the viscous component of the stress, **D** is the rate of deformation tensor, η_1 and η_2 are components of the fluid viscosity, λ is the longest relaxation time of the fluid, $\overset{\nabla}{\mathbf{T}}_1$ is the upper convected derivative, $\overset{\Delta}{\mathbf{T}}_1$ is the lower convected derivative, and ξ and ε are constant PTT parameters. Inertial terms were neglected because the Reynolds number for the least viscous fluid is $O(10^{-2})$. Surface tension was neglected as well because the capillary number is approximately 90.

The boundary conditions for the simulation are fully developed flow for each fluid at the inlet, no slip at the top and bottom walls of the channel, and a plane of symmetry

boundary condition where the rectangular cross-section was cut in half. A very small amount of slip is applied on the side wall to allow for the evolution of the interface as it moves downstream. Initially, all fluid-fluid interfaces were made flat and divide the rectangular cross section into equal area parts at the inlet. The normal and tangential forces are set to vanish at the outlet. Fluid-fluid boundaries were allowed to move in order to satisfy continuity of velocity, shear stress and normal forces applied at the fluid-fluid interface. This allows us to capture the changing shape of the fluid-fluid interface throughout the channel.

POLYFLOW© was used to perform the simulation. POLYFLOW© is a finite element package that can be used to simulate many different kinds of non-Newtonian flows, with a special focus on polymers. It is equipped with a graphical solid body modeling program and a graphical meshing program that was used to model the geometry and create the computational mesh. The solver packages used in this work are the Elastic Viscous Split Stress Method (EVSS) with Streamline Upwinding and Discrete Elastic Viscous Split Stress Method (DEVSS) with Streamline Upwinding. The EVSS method uses a substitution of variables to split the viscous stress from the elastic stress in order to increase simulation stability. Greater stability is achieved because this method keeps the problem from changing from an elliptic PDE to a hyperbolic PDE. The DEVSS method adds on to the EVSS method by treating the deformation tensor as an unknown variable. DEVSS is a very popular method as it is stable even at higher Weissenberg numbers. Streamline upwinding is a technique that applies stabilizing artificial diffusion along the

streamlines of the flow. This is done instead of the standard artificial diffusion because it is isotropic, meaning that the numerical diffusion distorts the solution in all directions, while the streamline upwinding distorts it only along the streamlines. The simulations are done by first solving the multi-fluid flow with still interfaces and using an evolution scheme on the wall friction factor and on the fluid relation times then importing the solution into a new simulation that evolves the interface taking the still flat interface solution as a starting point.

Either evenly distributed rectangular meshes or rectangular meshes that get smaller near the walls (biased rectangular meshes) were used for the finite element computations. Biased rectangular meshes were used to capture the behavior of fluid-fluid interfaces when they became very distorted and non-biased were used otherwise. The resulting finite element equations were solved using the EVSS method with Streamline Upwinding for the matching rheology pair computations and the DEVSS method with Streamline Upwinding for the mismatched pair because of its greater stability [Guenette and Fortin (1999)].

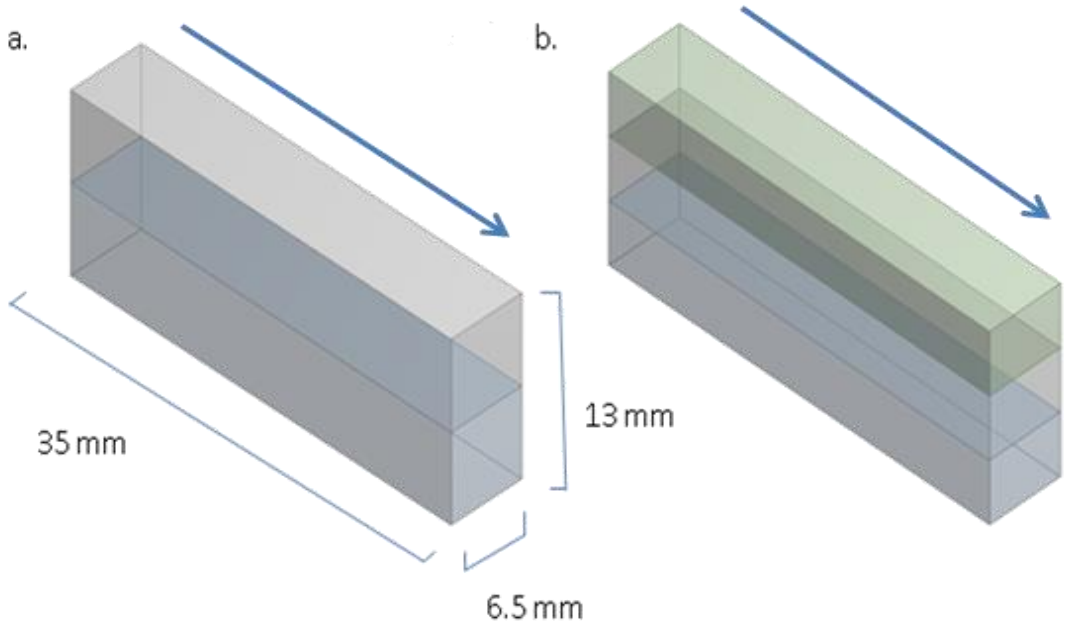

Figure 2.1: Feedblock geometry and initial interface locations for two (a) and three (b) layer flow. Blue arrows indicate the direction of flow in the channels.

The steady-state flow was solved using nested evolution schemes to ensure converged solutions. The quantities allowed to evolve were the side wall friction, the relaxation time, and the interface shape. The wall friction was increased until the velocity of the fluid at the wall was 1% of that in the center of the channel or less. The generalized Navier slip law was used where $f_s = kv_s$, where f_s is the tangential force at the wall, v_s is the tangential velocity and k is the slip constant. A mesh refinement was done to ensure converged solutions for these flows. Similar studies using different mesh sizes in similar geometries have also been conducted using the same code [Chabert (2011)], with similar results.

Two different pairings of polymers were simulated, with one pairing having similar rheology (*i.e.,* similar viscosities and relaxation times) and the other pair having mismatched rheology. The matched rheology pair is PMMA VS 100 with polystyrene (PS). The mismatched rheology pair is a polymethylmethacrylate designated PMMA VS 826 with polystyrene (PS). The full relaxation spectra of these materials were measured. The materials and their corresponding constitutive parameters are listed in Table 2.1. A plot of experimental rheological data and the fit based on the relaxation spectrum for each of the materials used are shown in Fig. 2.2. The agreement is very good. For each polymer in the simulation, only the longest relaxation time and the viscosities for the longest (η_1) and shortest (η_2) relaxation times were used since the flow is relatively slow and these parameters are sufficient to capture the salient features of the flow.

In a simulation, the volumetric flow rates of all materials were the same. The flow rates per layer for the two, four, six, and eight layer simulations were 300 mm^3/s, 150 mm^3/s, 100 mm^3/s, and 75 mm^3/s, respectively.

2.3 Experiments Performed by Collaborators

Prior to co-extrusion, all materials were dried for 24 hours at 80°C. Co-extrusion was performed at 230°C using two Killion extruders, model number 19782; and Zenith melt pumps, model number K46LP56. Screw RPMs were set to a constant 5.0 RPM. One of the polymer pairs was dyed to allow for visualization. Flow visualization was performed by stopping the flow and cooling the extruder. The multiplier die was opened and the solid material was sectioned and photographed.

Table 2.1: A table showing viscoelastic properties (viscosity, relaxation time, and PTT fitting parameters) for materials simulated and used in experiments. A letter is also included to show how materials are denoted in other plots (A, B, C).

Table 1: Phan-Thien Tanner Constitutive Parameters for Simulated Polymers						
Material and Designation	**η (Pa*s)**	**λ (s)**	**ξ**	**ε**	**Viscosity ratio**	
PMMA VS 100	25.0	5.96×10^{-5}	0.55	0.49	0.626	
A	93.9	6.22×10^{-4}				
	233.9	3.24×10^{-3}				
	308.7	1.36×10^{-2}				
	185.4	6.02×10^{-2}				
	15.0	7.85×10^{-1}				
PS	57.1	3.14×10^{-4}	0.51	0.07	0.557	
B	187.2	2.53×10^{-3}				
	337.7	1.26×10^{-2}				
	378.3	5.32×10^{-2}				
	219.7	2.33×10^{-1}				
	45.6	1.26×10^{0}				
PMMA VS 826	14.2	2.99×10^{-5}	0.34	0.47	0.015	
C	62.0	3.93×10^{-4}				
	312.6	2.35×10^{-3}				
	1142.0	1.12×10^{-2}				
	2799.6	5.12×10^{-2}				
	3730.8	2.24×10^{-1}				
	1727.1	1.03×10^{0}				
	912.3	9.22×10^{0}				

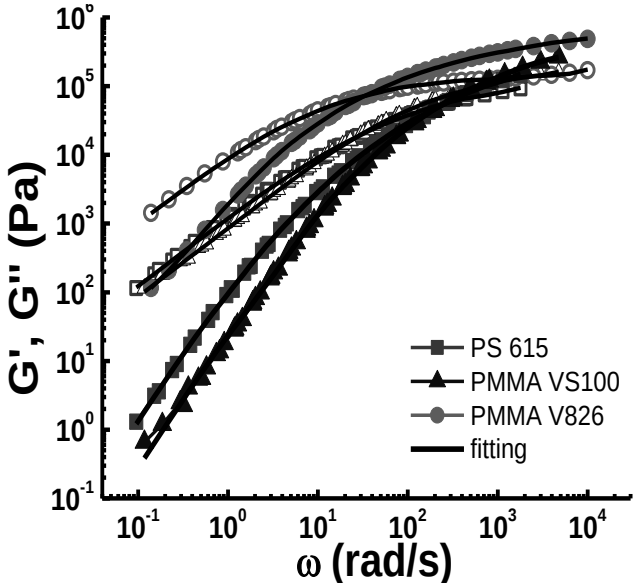

Figure 2.2: Viscous and elastic modulus data are plotted for the three materials being used. The solid lines through the data represent the relaxation spectra fit for these materials. The open symbols represent G'' values and the filled symbols represent G' values.

2.4 Results and Discussion

The first simulation performed was of two layer co-extrusion flows using a pair of polymers with matched rheology and another pair with mismatched rheology. Fig. 2.3 shows velocities and second normal stress differences for the matched and mismatched polymers throughout the feed block. The velocity profiles for both the matched and mismatched rheology show faster moving fluid at the center and zero velocity at the no-slip walls. The interface between the two fluids of matched rheology changes from a flat line at the entrance of the channel to a slightly distorted curve at the exit, while the mismatched fluids develop a much more strongly curved interface. The second normal stress differences for the matched rheology pair start out distributed somewhat unevenly,

but as the flow progresses toward the exit, its distribution becomes very symmetrical about the fluid-fluid interface and the differences are very small. The second normal stress differences for the mismatched pair start out somewhat evenly distributed about the interface, but as the flow approached the exit, the second normal stress differences become larger and very non-symmetrical about the interface.

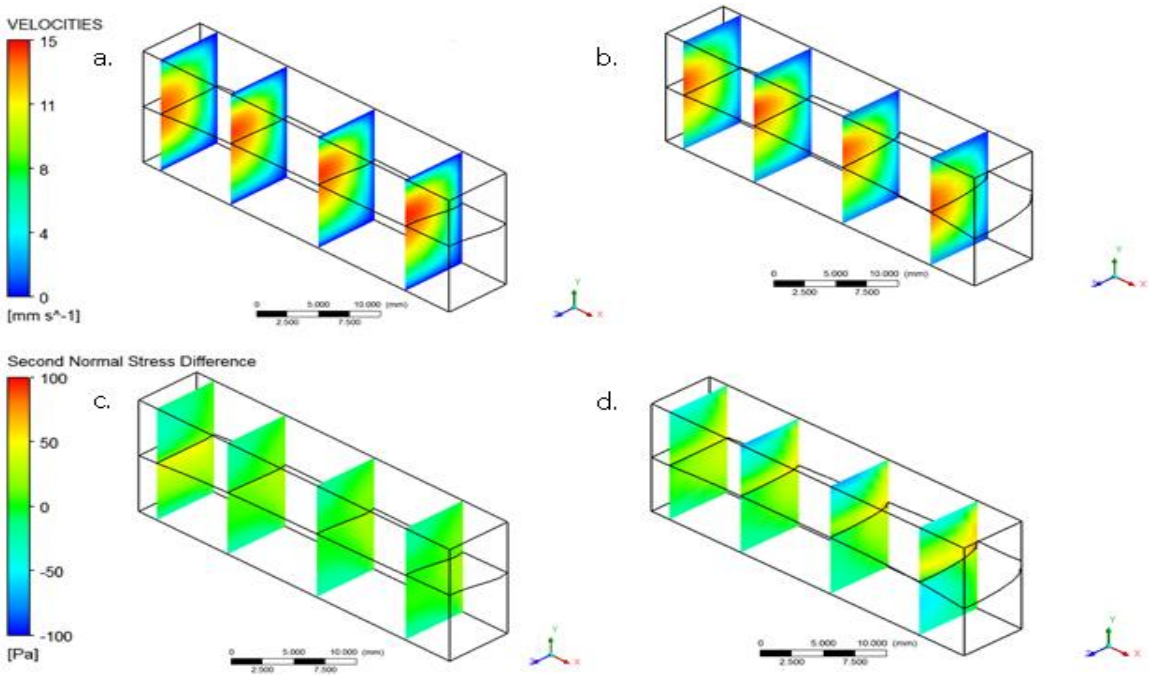

Figure 2.3: Velocity profiles for the matched and mismatched rheology pairs of polymer melts throughout the feedblock (a, b) and second normal stress differences (c ,d).

These simulations give insight into some very important aspects of the problem of interface stabilization. One is that greater interface distortion is seen in polymer pairs with mismatched rheologies. The interface distortion is also noted to slowly evolve along with

the second normal stress difference distribution from the beginning of the channel to the end. The effects of second normal stress differences on interface shape have been studied experimentally and numerically [Debbaut et al. (1997); Dooley (2002)]. Greater second normal stress differences and interface distortion are seen in the mismatched pairing than in the matched pairing.

Fig. 2.4 shows results from simulations and also compares the computed interfaces to those from experiments. The computed velocities of the fluids in the channel, second normal stress differences, and in-plane velocities are shown alongside photos of the experimental results. The simulations very accurately predict interface shape in all but one case. This case is the three layer configuration of the mismatched rheology pair in which the more viscous fluid is in the middle. This requires the simulation to merge interfaces, which it cannot do.

These results show a clear link between interface distortion, in-plane velocities, and second normal stress differences. The matched rheology pair is seen to have fewer locations with large second normal stress differences and in-plane velocities that go in all directions. These cancelling in-plane velocities and lower stresses lead to less rearrangement of the fluids and, consequently, less interface distortion. In contrast the pair with mismatched rheology has large second normal stress differences concentrated in different areas and more unidirectional in-plane velocities and thus has a great deal of interface distortion. It is also seen that increasing the number of layers from two to three with the mismatched pair helps stabilize the interfaces if the layering is such that the second

normal stress differences are spread out and decreased in magnitude like in the three layer simulation with the less viscous fluid in the middle.

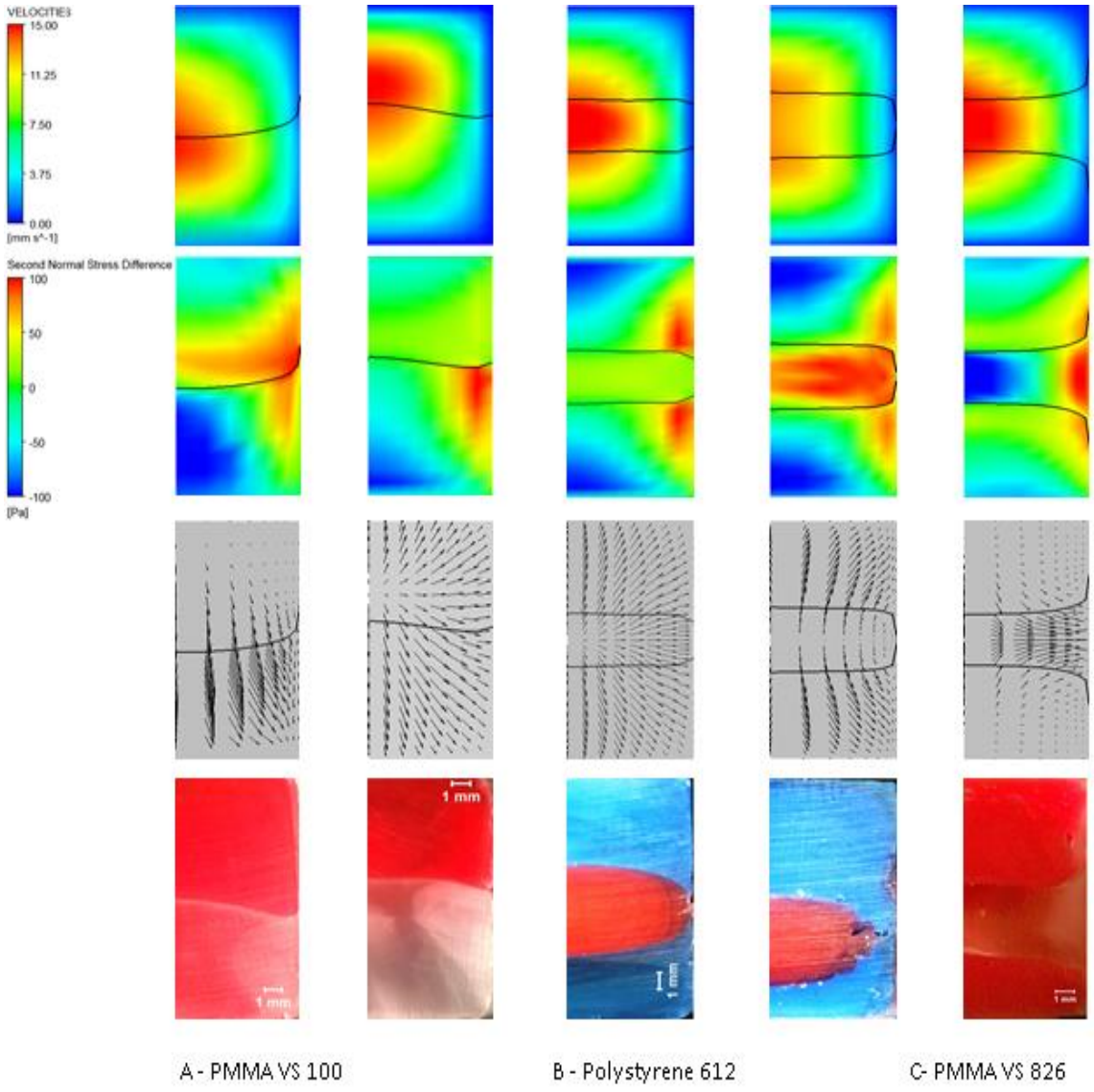

Figure 2.4: Columns depict the same experiment, while rows show the same type of information. From left to right, experiments are of the following materials C-B, A-B, B-A-B, B-C-B, and C-B-C. From top to bottom, total velocities, second normal stress differences, in-plane velocity vectors, and photos of actual experiments for comparison.

The effects of viscous and elastic forces on encapsulation have been investigated previously [Dooley and Rudolph (2003)]. Viscous forces have been determined to be less important at the exit of the feedblock because the second normal stress differences persist throughout the feed block and continuously change the shape of the interfaces while the viscous forces change relatively little across the feedblock. It is expected that these second normal stress differences will also continue to distort the interfaces downstream from the feedblock.

From the results depicted in Figs. 2.3 and 2.4, two potential methods for reducing interface distortion present themselves. The first strategy is to add more layers to spread the second normal stress differences throughout the channel, thereby lessening their effect on a single interface as seen in Fig. 2.4. The idea of introducing several layers into the feed block has been explored experimentally and numerically in other works [Perdikoulias (1995); Dooley (2010)] and has been used in industry [Wagner (2010)], but the mechanism behind its ability to help stabilize the interfaces and its influence on the second normal stress differences have not been fully described. The second strategy is to decrease the friction at the walls of the channel. This is suggested by how second normal stress differences develop and grow as the flow progresses in Fig. 2.3d. The first of these methods is explored by simulations shown in Figs. 2.5 and 2.6 and the second in Fig. 2.7.

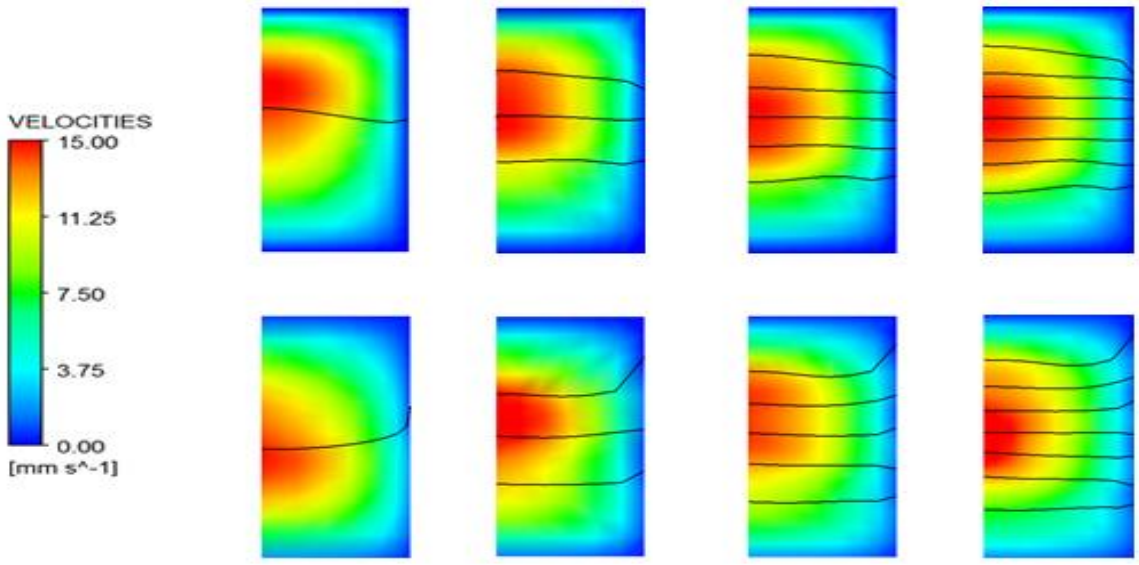

Figure 2.5: Velocities and interfaces of polymer melts as they leave the rectangular die. Matched viscosity pairings are seen on top and mismatched viscosity pairings are on the bottom.

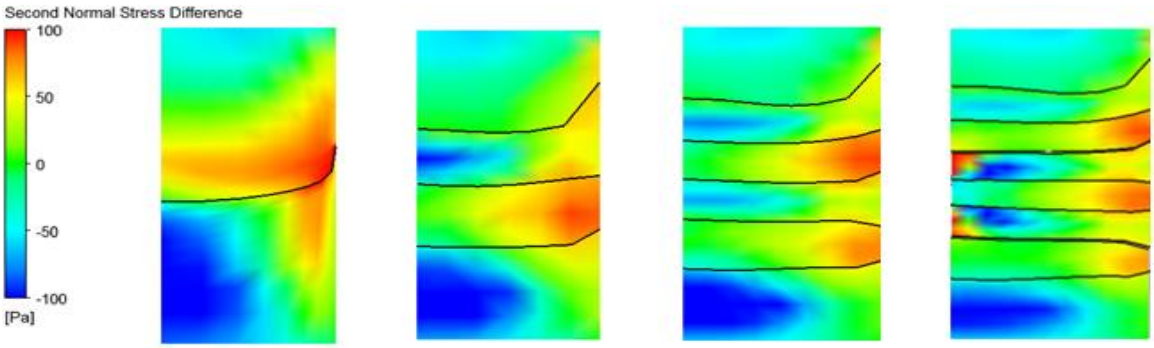

Figure 2.6: Second normal Stress differences for the mismatched rheology pairing. The number of layers increases from left to right going from two to eight layers.

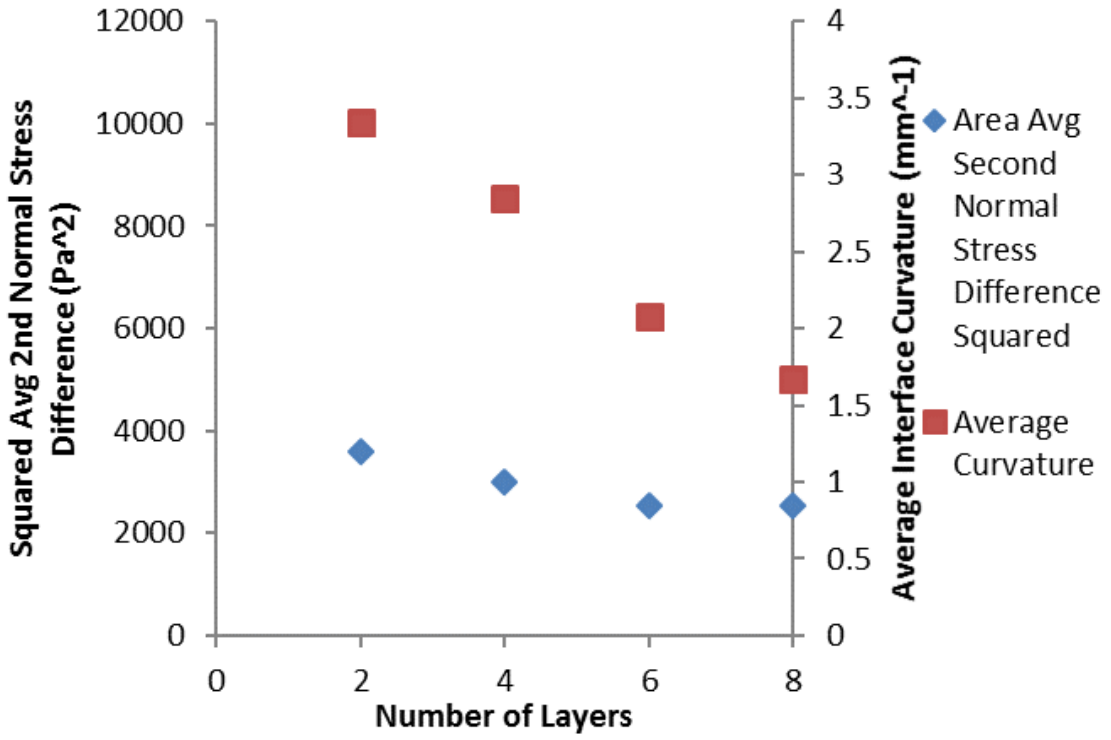

Figure 2.7: The squared second normal stress differences are averaged over the outlet of the die and plotted on the left y axis against the number of layers. The average interface curvature is plotted on the right y axis against the number of layers.

In Fig. 2.5, the output interface shapes and velocity profiles are given for two, four, six, and eight layer configurations for both the matched and mismatched polymer pairs. As the number of layers increase, both pairs show increasingly flatter interfaces. For both pairings, the top and bottom interfaces tend to show the greatest distortion, with central interfaces being flatter. Fig. 2.6 shows how second normal stress differences change at the feed block exit with number of layers for the mismatched pair. The layers begin to alternate showing a strong negative difference on the left in one layer and a strong positive difference on the right in the next layer below it.

The results in Figs. 2.5 and 2.6 demonstrate that, while the top and bottom interfaces may remain somewhat distorted, the center interfaces are much flatter. This is attributable to the greater distribution of second normal stress differences throughout the plane in the configurations with more layers. Thus, the two layer configurations have concentrated zones of very high second normal stress differences and the worst distortion, while the eight layer configurations have high and low second normal stress differences well distributed throughout the exiting normal plane with layers of less viscous fluid and lower relaxation time sitting between the layers of very viscous fluid and high relaxation time. This dispersion causes in-plane flows to be smaller, due to the smaller layers and more directions the fluid is pulled in. The average curvature of the interfaces and the average of the squared second normal stress differences are plotted against the number of layers in Fig. 2.7. This shows that the eight layer flow configuration having the least distortion of any of the different layering configurations.

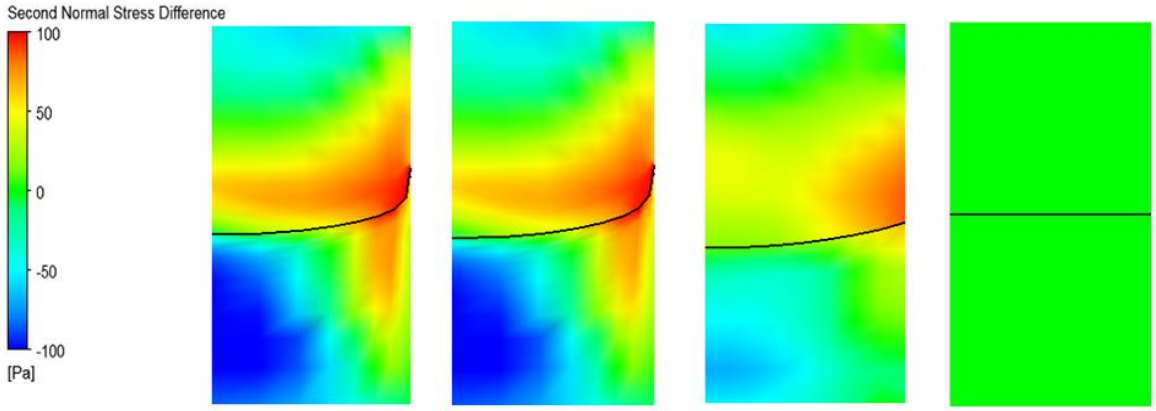

Figure 2.8: Interfaces and second normal stress differences for the mismatched rheology pairing as it leaves the rectangular die under various amounts of wall slip. Seen from left to right, approximated no slip condition corresponding to k=120,000 (velocity at the wall is 1% or less of the velocity in the center of the die), three fourths wall friction k=90,000, one sixth wall friction k=20,000, and no wall friction k=1.

The results in Fig. 2.8 explore the second strategy discussed for mitigating interface distortion, namely to increase fluid slip along the walls of the feed block. Second normal stress differences at the exit of the feed block are shown. There is a great deal of contrast in the values of these differences around the interface in the no-slip case. The interface is also very distorted. When the wall friction is reduced to three quarters of the no-slip value, there is no change observed in either the interface or the second normal stress differences. However, when the wall friction is reduced to a sixth of the no-slip value, the second normal stress differences map shows much smaller differences and interface distortion is reduced. Finally, when there is no wall friction, the interface is perfectly flat and all second normal stress differences vanish. Fig. 2.9 shows a plot of interface curvature and average

squared second normal stress differences at the outlet plotted against the wall friction parameter k.

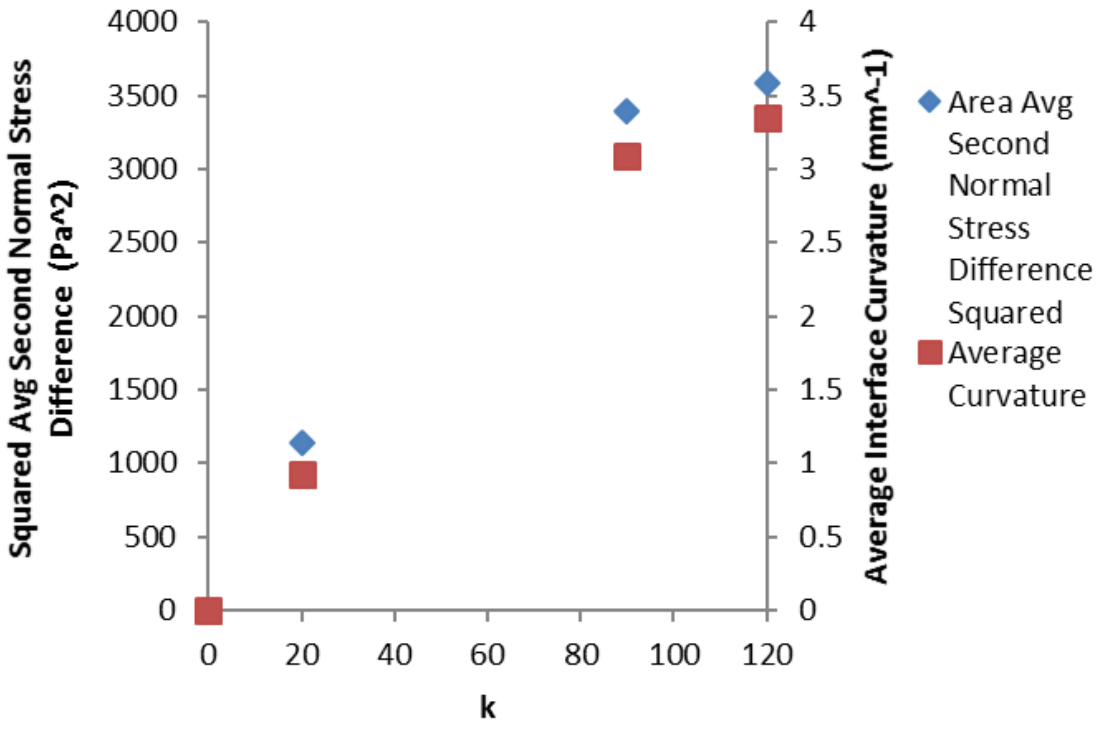

Figure 2.9: The squared second normal stress differences are averaged over the outlet of the die and plotted on the left y axis against the wall friction parameter, *k*. The average interface curvature is plotted on the right y axis against *k*.

Decreasing wall friction below some critical value dramatically reduces second normal stress differences and interface distortion in the co-extruded product. The results of

these simulations show that reducing wall friction is a viable means of reducing or eliminating interface distortion, provided that the wall friction can be made to be below a certain critical value.

2.5 Conclusions

We have demonstrated and analyzed different methods to reduce interface distortion in multilayer co-extrusion in a channel of rectangular cross-section. Simulations performed were shown to correlate well to experiments by comparing the distortion of the output interfaces for materials with matched and mismatched rheologies. Second normal stress differences in the fluids were found to correlate with increased in-plane flows and increased interface distortion in these simulations.

Two methods of handling these second normal stress differences were explored and shown to be effective in reducing interface distortion. The first was to better distribute the second normal stress differences throughout the channel cross-section by adding more layers. This was seen to distribute the second normal stress differences and makes for much improved layers with the flattest in the center while the top-most and bottom most layers are more distorted. The second method was to greatly reduce the second normal stress differences by decreasing the wall friction. Decreasing wall friction was found to be very effective in eliminating interface distortion, with perfectly flat layers produced an all second normal stress differences vanishing when wall friction force is zero. Wall friction must be reduced substantially, however, in order to have any effect on the layer shape.

Using these two methods, it is recommended that the feed block start with as many layers fed to it as possible and that the walls of the feed block offer very little resistance to the flow of polymer. We suggest that future work should be to experiment with very slippery surfaces in the feed block. We also suggest that more layers be introduced to the feed block in an attempt to gain even greater interface stability.

Chapter 3: Design of Co-extrusion Multiplier Dies

3.1 Introduction

Multiplier dies are critical to the structure formation process of multilayer polymers. Each die doubles in the number of layers. The layer multiplier dies work by dividing the flow into two symmetrical channels that eventually converge together again placing one flow on top of the other, doubling the number of layers, as seen in Fig. 3.1. There are two issues to address when designing multiplier dies. The first is that pressure drops through these dies can be quite high and needs to be minimized. Higher pressure drop forces larger equipment sizes and puts more stress on the extruder. The is because the higher pressure drops re[2]quire more powerful screw extruders and also more bolts of larger size to hold the equipment together as these high The second issue is that the design of the multiplier die impacts quality of the interfaces and negative impact needs to be reduced. The original multiplier die increases interface distortion by having large areas of the die influenced by wall shear. This wall shear creates second normal stress differences which result in fluid motion perpendicular to the direction of co-extrusion.

Interface deformation in co-extrusion processes has been explored by Anderson et al. (2006). Viscous and elastic encapsulation are important processes in the multiplier die

---

[2] Material in this chapter published in:
Huang, R., et al. (2015). Co-Extrusion Layer Multiplication of Rheologically Mismatched Polymers: A Novel Processing Route. *International Polymer Processing*, *30*(3), 317-330
Harris, P. J. et al. (2014). Improved interfacial surface generator for the co-extrusion of micro-and nanolayered polymers. *Polymer Engineering & Science*, *54*(3), 636-645. I did all the simulations and their analysis for the parts of the works shown.

[Dooley (2002); Hatzikiriakos et al. (2005); Torres et al. (1993); Borzachiello et al. (2014); Yue et at. (2008)]. In this chapter, the performance of two different dies are compared in terms of interfaces generated and pressure drop. As in the previous study, two material pairs, one with matched rheology and one with mismatched rheology are simulated. Collaborators at Case Western Reserve University provide experimental results.

3.2 Simulation Method

The simulation method and material properties of the polymers are similar to the one in Chapter 2. The primary difference is the domain in which the equations are solved. In this study, multiplier die geometries are simulated instead of the simple feedblock geometry. From these simulations, we can observe die performance in different metrics and compare across designs. The two primary metric of interest are the pressure drop needed to push materials through the die at the same volumetric flow rates and the quality of the interface generated. The quality of interface generated is a qualitative assessment that looks primarily at the degree of layer encapsulation and curvature along with general deviation from the perfectly flat layered structure that is desired.

A new multiplier design is proposed in Fig. 3.1. The original multiplier die has a vertical contraction step followed by an expansion step. The second-generation die is designed to keep the cross-sectional area of constant to try to reduce the pressure drop that results from the bottleneck in the original design. By avoiding this bottleneck, the high pressure drop to push fluids through this bottle neck is also avoided. The new design also includes a section where the cross-sectional geometry remains constant so as to allow the

polymer to relax before entering the next multiplication step. This relaxation step should help reduce flow from elastic forces within the fluid. The die design was proposed by collaborators at Case Western Reserve University and I did the simulations and testing. Fig. 3.1 shows a side-by-side comparison of the new multiplier die design with the original design.

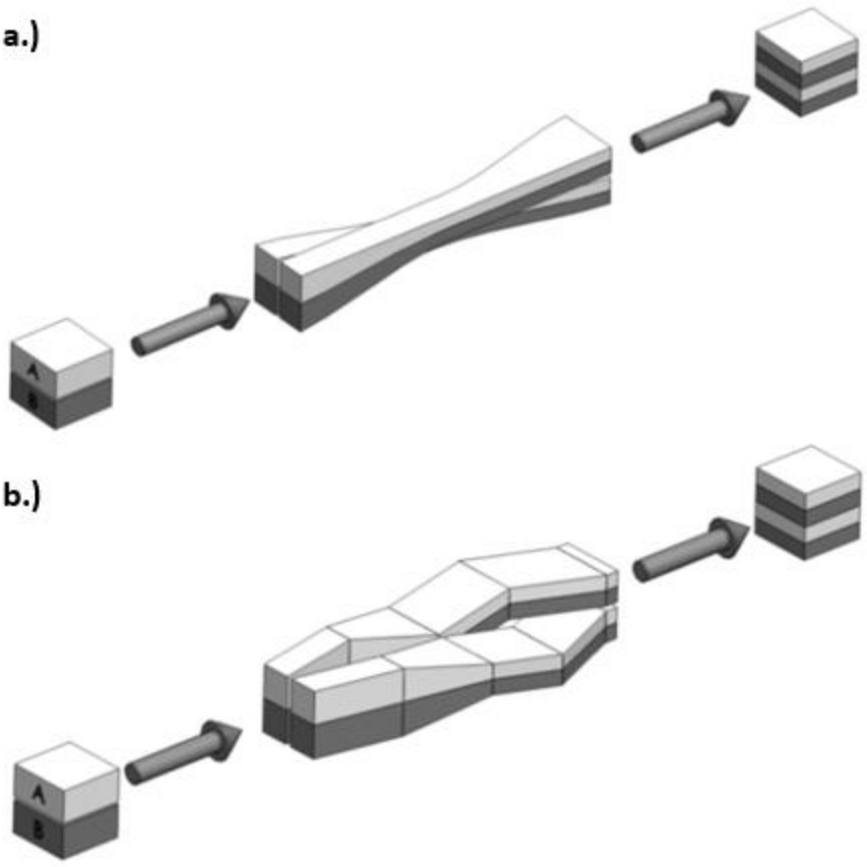

Figure 3.1: Two fluids, A and B, are shown going through different multiplier die designs. The original design (a) has a vertical contraction step followed by a horizontal expansion step and is done smoothly across the length of the die. The second generation die (b) does the horizontal expansion and vertical contraction simultaneously near the channel entrance keeping the cross sectional area constant. Near the exit of (b) there is a stretch of no change to allow relaxation of the polymers.

The second design goal is to improve the quality of the co-extruded product by increasing layer flatness. This is explored in simulations of dies that are flat and thin. Fig. 3.2 depicts this type of multiplier die.

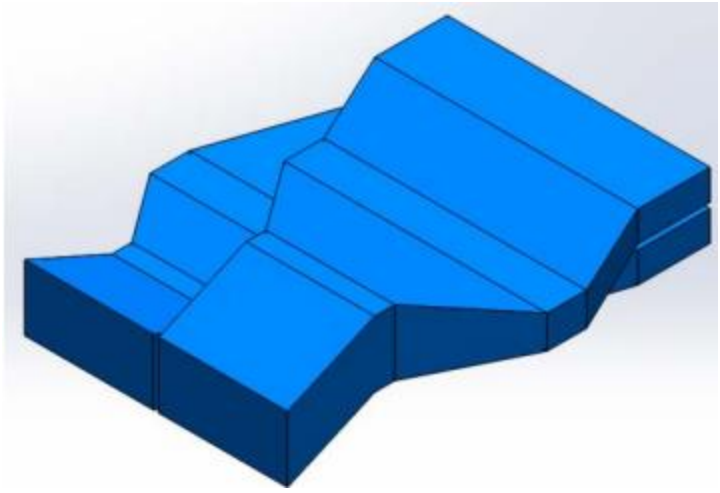

Figure 3.2: High aspect rectangular multiplier dies are shown.

This die design seeks to minimize velocity vectors normal to the direction of extrusion by reducing the wall shear near the channel center. This is done by pushing the side walls out as far as possible using a rectangular die cross-section. Details of the accompanying experimental results performed by collaborators at Case Western Reserve University for the pressure drop reducing die [Harris et al. 2014] and the high aspect rectangular dies [Huang, R., et al. 2015] can be found in other publications.

3.3 Results and Discussion

3.3.1 Pressure Drop Reducing Design

To make a relevant comparison between the two dies, both dies were simulated using three different layer configurations of three layer flow cases. These cases were using the matched rheology pairing (PMMA vs100 and PS) with the more viscous polymer in the middle and the mismatched rheology pairing (PMMA vs826 and PS) with less viscous

in the middle and a final case with the more viscous fluid in the middle. Fig. 3.3 shows the velocity profiles from these simulations.

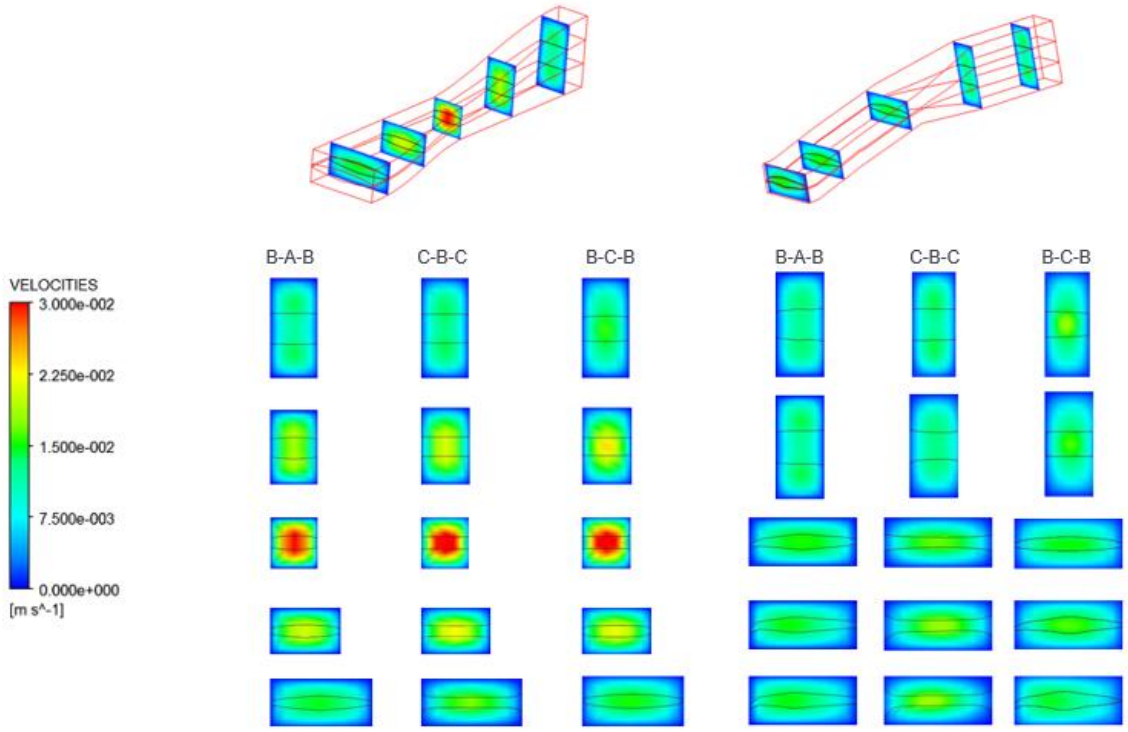

Figure 3.3: Velocity profiles for each of the configurations tested. The previous multiplier die is shown on the left and the second generation die is on the right. The letters in each column of panels indicate how the materials are configured in the channel from bottom to top. Letter "A" denotes PMMA vs100, "B" denotes PS, and "C" denotes PMMA vs826.

The velocity profiles show the expected trends. The original multiplier die has velocities that are faster near the contraction while the newer die has very similar velocity profiles throughout the channel because the cross-sectional area remains constant. The pressure drop across the channel was also calculated from the simulation results. Fig. 3.4 reports the pressure drops for each die in various flow configurations.

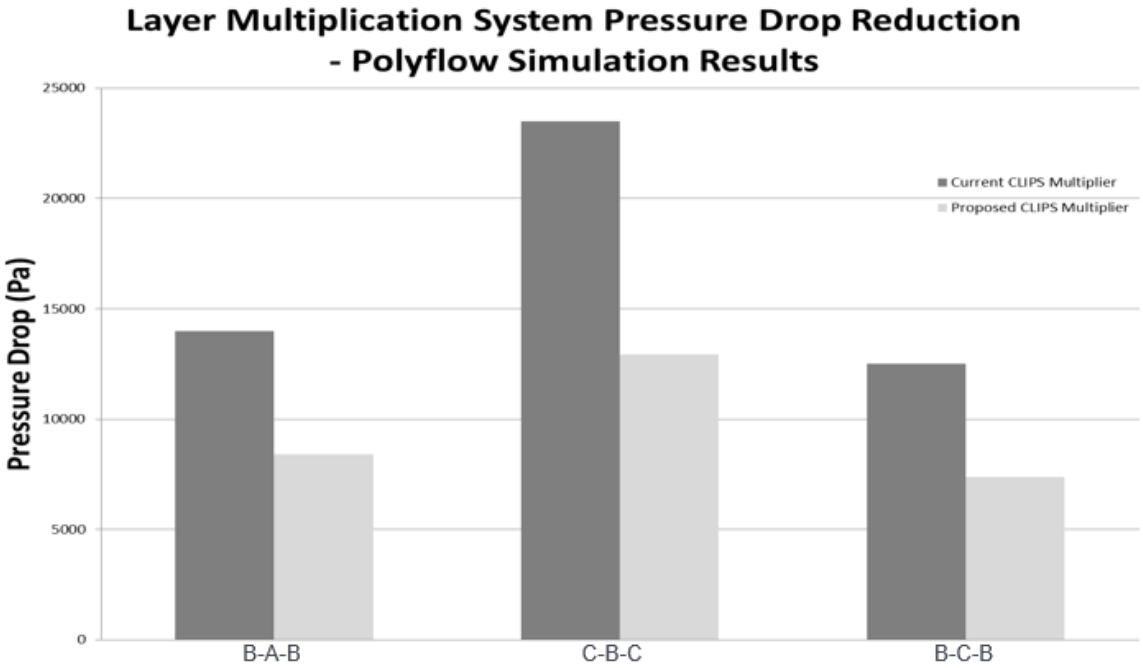

Figure 3.4; Pressure drops are shown for each configuration shown along the x axis. The new multiplier die reduces the required pressure by about 40% across all flow configurations.

The second normal stress differences were also calculated from the simulation results. These results are shown in Fig. 3.5. The exiting interfaces in each case, when compared between the original die and the improved die, are qualitatively the same. Encapsulation is seen in both cases where the more viscous fluid is in the middle and the less viscous fluid is on the outside. The degree of encapsulation appears to be qualitatively the same as well.

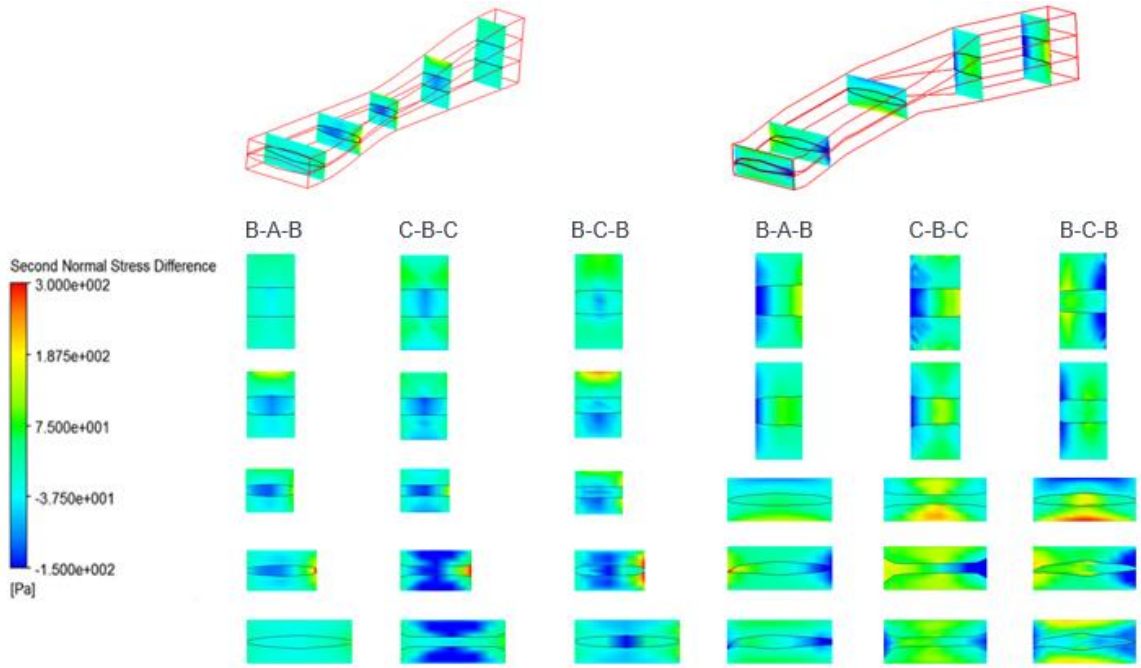

Figure 3.5: Second Normal Stress differences plotted for each of the three flow configurations in each of the multiplier die designs. The older design is shown on the left and the newer one is shown on the right.

3.3.2 Rectangular High Aspect Ratio Dies

The second design tested is a high aspect ratio die designed to minimize interfacial deformation. A nine layer flow case with the rheologically mismatched pair was simulated in this type of die. Fig. 3.6 shows the results of this simulation.

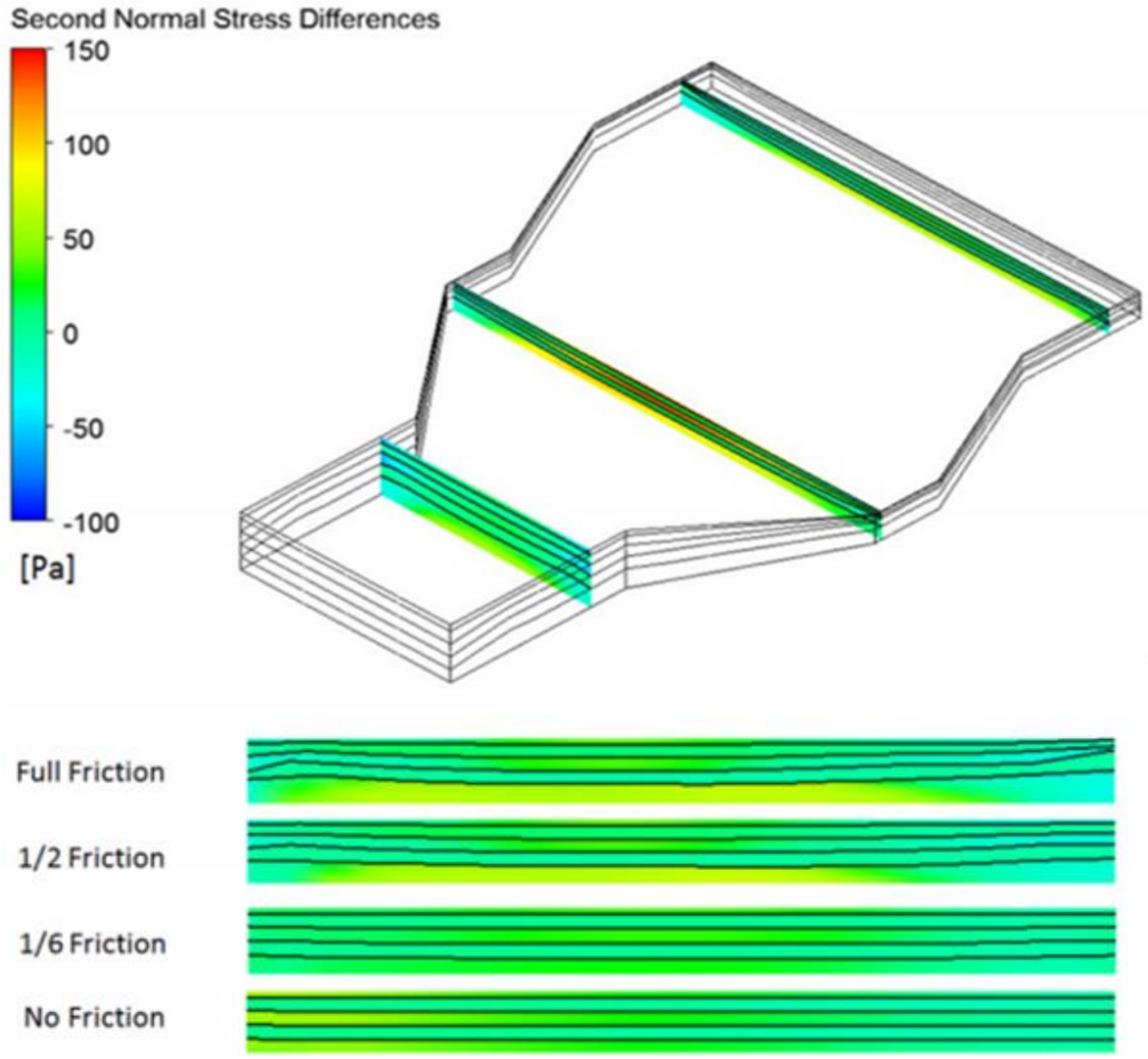

Figure 3.6: Simulation of a nine layer flow case with the mismatched rheology pair is shown. To reduce computation time, a symmetry boundary condition was used in the channel center so only 4.5 layers are seen. Second normal stress differences are plotted with a color scale in three separate planes. The bottom shows exit panels from simulations where reduced wall friction parameters were used.

The results shown in Fig. 3.6 show that in the full friction case interface deformation is mostly localized near the side walls and flatter layers are more prominent

in the center of the channel. As friction is reduced, the deformation near the side walls is also reduced. Once wall friction is completely eliminated, interfaces are perfectly flat all the way across the die exit.

3.3.3 Experimental Results from Collaborators

The designs explored in this work that were found to be promising were experimentally tested by collaborators at Case Western Reserve University. The details of their experiments can be found in [Harris et al. (2014); Huang et al. (2015); and Huang (2014)]. The polymers were dyed different colors in the experiment and their cross-sections were examined in order to observe their layering. Fig. 3.7 shows the pictures taken in these experiments.

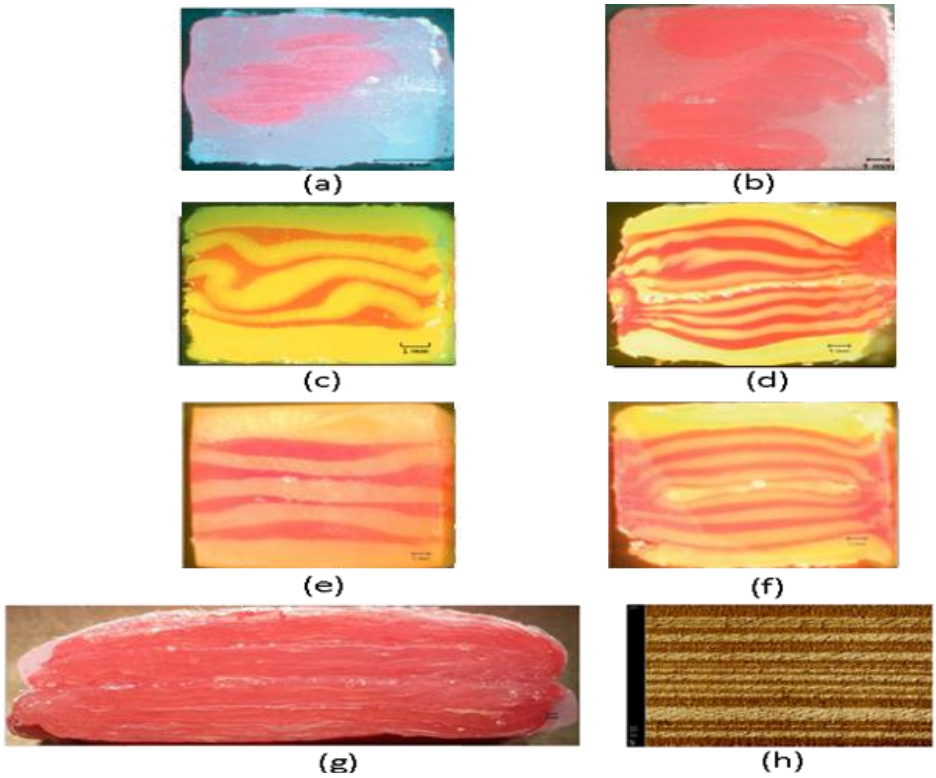

Figure 3.7: All experiments are done with polyurethanes with visco-elastic ratio of 100. (a) and (b) show a nine layer structure and 17 layer structure, respectively, created using the original feed block and multiplier die. (c) and (d) show the same number of layers as created by the new feed block and multiplier die (for reduced pressure drop). (e) and (f) show 9 and 17 layers in the new feed block and multiplier dies using slip agents to reduce wall shear. (g) shows a 1025 layer structure created using slip agents and the high aspect ratio die. (h) is an AFM image of (g).

Fig. 3.7 shows that as the improvements are added (slit dies, slip agents, and pressure drop reducing dies) the interface flatness is preserved better and better. Finally, when slit dies are added, the interfaces are shown to be flat even down to the scale measured by the AFM in Fig. 3.7(h).

3.4 Conclusions

We have explored, through simulation, two different improvements for the design of multiplier dies in this co-extrusion process. The first design successfully reduced the pressure drop in the three flow configurations tested by 40% as compared to the original multiplier die design. The second design successfully implemented a high aspect ratio design to improve the interface flatness in the final layered structure.

The first proposed design change was to decrease the required pressure drop over the original die design. This was done by keeping the cross-sectional area of the die constant in order to avoid the bottleneck created in the original design. This successfully lowered the pressure drop in the simulation by 40% for all cases tested.

The second proposed design used high aspect ratio rectangular cross-sections to minimize the wall shear, and thus second normal stress differences, near the side walls. This results in in-plane rotational flows that disrupt the layered structure being localized near the side walls and leaving flatter interfaces in the center of the die. The layer flatness is improves even further still when flow lubricants are added. This decreases interface deformation at the side walls and also allows the fluid to travel at a more constant velocity within the plane which leads to layers of more uniform thickness.

Our collaborators at Case Western Reserve University tested these designs experimentally and their results show that these design changes greatly improve layer quality. The high aspect ratio die coupled with the flow lubricants preserves the layered

structure even when the number of layers reaches 1025. AFM images show that layer flatness is preserved, even on a very small scale.

Chapter 4: Stability of Visco-Plastic Flow Down an Inclined Plane

4.1 Introduction

In this chapter the analysis of the stability of the flow of a soft particle paste down an inclined plane is performed. This problem is of particular interest as it is a stability problem that is related to roll-to-roll processing of soft particle pastes, which is explored in the following chapter. Yih first studied the problem of stability of a falling Newtonian liquid film [Yih, C., (1955)]. Since then, many researchers have analyzed the stability of different materials flowing on an inclined plane. This includes visco-elastic materials [Gupta, A. S., 1967], power law fluids [Hwang, C., (1994)], and for a material with a highly non-linear constitutive equation [Yih, C., (1965)]. Stability of flows of many other materials have also been considered [Malloggi, F., et al., (2015); Allouche, MH., et al. (2015); Richard, GL., et al. (2016)]. The paste in this problem has both a yield stress and a second normal stress difference. The shear stress and shear rate relationship is given by the Herschel-Bulkley model. This second normal stress difference is hypothesized to be a source of instability when there is a transverse disturbance in the free surface of the material. A schematic of this problem is shown in Fig. 4.1.

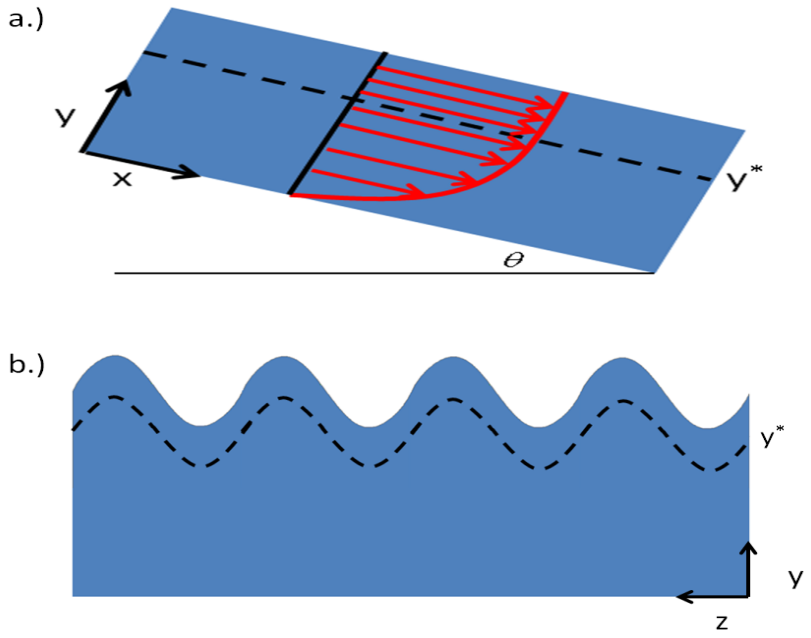

Figure 4.1: a) A diagram of the inclined plane flow problem. The base flow field is the red line and vectors in the diagram. The line y* is the yield point in the flow, everywhere above that point moves as a solid. In b), the perturbation to be analyzed is shown. The wave penetrates through the solid part of the material on top down to the region where flow occurs.

4.2 Theoretical Analysis

4.2.1 Base Case Problem Set Up

Flows considered in this analysis are incompressible and at low Reynolds number. Thus the field equations that need to be solved are

$$\nabla \cdot \boldsymbol{\tau} + \rho \boldsymbol{g} = 0, \tag{4.1}$$

$$\nabla \cdot \mathbf{u} = 0, \tag{4.2}$$

where ρ is the fluid density, g is the gravitational acceleration, $\mathbf{u}$ is the velocity vector field, and $\boldsymbol{\tau}$ is the stress tensor. The Herschel-Bulkley constitutive law is then used to relate stress to strain rate as given in Equation 4.3, namely,

$$\boldsymbol{\tau} = \left(k_1 \left| \dot{\gamma} \right|^{-\frac{1}{2}} + \frac{\tau_0}{\left| \dot{\gamma} \right|} \right) \dot{\boldsymbol{\gamma}} \quad , \qquad \tau > \tau_0 \tag{4.3}$$

$$\left| \dot{\gamma} \right| = \sqrt{\frac{1}{2} \sum_{i,j} \dot{\gamma}_{ij} \, \dot{\gamma}_{ij}} \, , \tag{4.4}$$

$$\dot{\boldsymbol{\gamma}} = \frac{1}{2} \left(\nabla \mathbf{u} + \nabla \mathbf{u}^{T} \right) \tag{4.5}$$

where k_1 is a coefficient, τ_0 is the yield stress, and $\dot{\boldsymbol{\gamma}}$ is the shear rate tensor. For the base case flow, the flow is assumed to be unidirectional and parallel to the inclined plane. The resulting governing equations for the flow is then given by

$$\frac{d}{dy} \left(k_1 \left(\frac{du_x^0}{dy} \right)^{1/2} + \tau_0 \right) = -\rho g \, \mathrm{Sin}(\theta) \, , \tag{4.6}$$

with boundary conditions at

$$u_x^0 \left(y = 0 \right) = 0 \, , \tag{4.7}$$

$$\frac{du_x^0}{dy} \left(y = y^* \right) = 0 \, , \tag{4.8}$$

where y^* is the fluid thickness above which the paste behaves as a solid, θ is the angle of incline, and u_x^0 is the base case steady state velocity profile in the x direction. The paste

must behave as a solid once the shear stress drops below the yield stress, which is why y^* is the boundary of the fluid domain and not the free surface. The material also has a second normal stress difference as given by the empirical relationship:

$$\frac{N_2}{\tau_0} = -\left| N_{2,0} + k_2 \left(\left| \dot{\gamma} \right| \right)^{1/2} \right|, \tag{4.9}$$

where N_2 is the seccond normal stress difference, $N_{2,0}$ is a shear rate independent second normal stress difference, and k_2 is a constant coefficient. These equations are solved for the base case flow initially.

4.2.2 Perturbation Problem Set-up

Once the base case velocity profile is known, a perturbation is applied to the interface in the plane perpendicular to the flow. This affects the velocity, pressure, and shear stress fields, as shown in Equations 4.10-4.12

$$\boldsymbol{u} = u_x^0(y)\boldsymbol{e}_x + \boldsymbol{u}' \ , \tag{4.10}$$

$$P = P' \ , \tag{4.11}$$

$$\boldsymbol{\tau} = \boldsymbol{\tau_0} + \boldsymbol{\tau}', \tag{4.12}$$

where $\boldsymbol{e}_x$ is the unit vector in the x-direction, $\boldsymbol{u}'$ is the perturbed velocity field, P is the total pressure field, P' is the perturbed pressure field, $\boldsymbol{\tau_0}$ is the base case stress tensor, and $\boldsymbol{\tau}'$ is the perturbed stress tensor. When these perturbed equations are plugged into Equations 4.1 and 4.2 the following perturbation equations are arrived at

$$\frac{\partial \tau_{yz}^{'}}{\partial y} - \frac{\partial P^{'}}{\partial z} = 0, \tag{4.13}$$

$$P^{'} = -\gamma_{st} \frac{\partial^2 \eta}{\partial z^2}, \tag{4.14}$$

$$\frac{\partial u_y^{'}}{\partial y} = -\frac{\partial u_z^{'}}{\partial z}, \tag{4.15}$$

and then also yielding the boundary conditions

$$u_y^{'}(0) = 0, \tag{4.16}$$

$$\frac{\partial u_y^{'}}{\partial y}(0) = 0, \tag{4.17}$$

where $\tau_{yz}^{'}$ is the perturbed stress tensor component in the plane perpendicular to the direction of the steady state flow(y-z plane), P is the perturbed pressure field, η is the interface shape (as shown in Fig. 4.1 (b)), $u_y^{'}$ is the perturbed y velocity, $u_z^{'}$ is the perturbed z velocity, and γ_{st} is the surface tension. Equation 4.13 is from a simplification of the Cauchy stress balance equation and Equation 4.14 is the relationship between the perturbed fluid pressure and the surface tension forces resulting from the curved interface. To solve this perturbation problem, a sinusoidal perturbation is assumed of the form

$$\eta = \eta_0 e^{ikz+st}, \tag{4.18}$$

$$\boldsymbol{u}^{'} = \hat{\mathbf{u}}(y) e^{ikz+st}, \tag{4.19}$$

where k is the wave number, s is the growth rate, t is time, and $\hat{\mathbf{u}}(y)$ is the part of the perturbed velocity that depends only on y. Once the solution to this is obtained, it can then be plugged in the kinematic condition to order O(η) which is given by

$$\frac{\partial \eta}{\partial t} = u_y'(y^* + \eta). \tag{4.20}$$

Once the velocity is plugged into the kinematic equation for the interface, the stability of the interface can be determined.

4.3 Results and Discussion

First, the base case solution must be obtained. The base case flow has two regions, one below the yield point, y^*, where velocity is a function of y and one above the yield point where the material behaves as a solid and moves with a constant velocity that is not a function of y. This is a consequence of the fact that shear stress is a function of y and some of the material experiences a shear stress that is less than the yield stress, thus leading to some material behaving as a fluid and other material behaving as a solid. The thickness of the fluid region is found by a stress balance between gravity forces and the yield stress. The value of the yield point, y^*, is given by

$$y^* = d - \frac{\tau_0}{\rho g Sin(\theta)}, \tag{4.21}$$

where d is the overall film thickness and the two piece velocity profile is given by

$$u_x^0 = 1/3\left(\frac{\rho g Sin(\theta)}{k_1}\right)^2 \left[y^{*3} - \left(y^* - y\right)^3\right] \qquad y < y^*, \tag{4.22}$$

$$u_x^0 = 1/3\left(\frac{\rho g Sin(\theta)}{k_1}\right)^2 y^{*3} \qquad y > y^* . \tag{4.23}$$

Now that the base case solution is obtained, the perturbation problem must now be solved. The shear rate for the base problem is taken to be the average of the shear rate for mathematical convenience. This average shear rate is given by

$$\left|\dot{\gamma}\right| = C_{eq} = \frac{2q_0}{y^{*2}} \ , \tag{4.24}$$

$$q_0 = \int_0^{y^*} u_x^0(y)dy \ , \tag{4.25}$$

where C_{eq} is the average shear rate, q_0 is the flow rate of the liquid portion of the flow in the base case problem. The problem defined by Equations 4.13 through 4.17 now must be solved. The solution to this problem is given by

$$u_y = \frac{1}{6}(-3\frac{\tau_0\left(N_{2,0} + k_2 C_{eq}^{\ 1/2}\right)C_{eq}\eta_0}{\left(\tau_0 + k_1 C_{eq}^{\ 1/2}\right)}k^2y^2 - 3(y^* + \eta)\frac{\gamma_{st}\eta_0}{\left(\frac{\tau_0}{C_{eq}} + \frac{k_1}{C_{eq}^{1/2}}\right)}k^4y^2 + \frac{\gamma_{st}\eta_0}{\left(\frac{\tau_0}{C_{eq}} + \frac{k_1}{C_{eq}^{1/2}}\right)}k^4y^3), \tag{4.26}$$

and then this result is used in Equation 4.20 to yield the following expression for the wave growth rate,

$$s = \frac{1}{6}(3\frac{\tau_0\left|N_{2,0} + k_2 C_{eq}^{\ 1/2}\right|C_{eq}}{\left(\tau_0 + k_1 C_{eq}^{\ 1/2}\right)}k^2y^{*2} - 2\frac{\gamma_{st}}{\left(\frac{\tau_0}{C_{eq}} + \frac{k_1}{C_{eq}^{1/2}}\right)}k^4y^{*3}). \tag{4.27}$$

Instability is predicted for wave numbers that result in a positive value for s and stability is predicted for wave numbers that result in a negative value of s. The condition on k for stability is given by Equation 4.28

$$k \geq \sqrt{3\frac{\tau_0 \left| N_{2,0} + k_2 C_{eq}^{1/2} \right|}{2\gamma_{st} y^*}}\,, \tag{4.28}$$

Values of k smaller than those in (4.28) are found to be unstable. The relevant material properties for this problem are the second normal stress differences and the surface tension. A competition between these forces determines whether the instability will be stable or unstable. Larger values of surface tension help to stabilize the flow while larger values of the second normal stresses tend to destabilize it. The fastest growing mode of the instability was determined to be (4.29) and is also dependent on these same properties.

$$k_{\max} = \sqrt{3\frac{\tau_0 \left| N_{2,0} + k_2 C_{eq}^{1/2} \right|}{4\gamma_{st} y^*}} \tag{4.29}$$

The following variables are defined to conveniently report the results non-dimensionally:

$$\bar{s} = s\frac{\left(\tau_0 \left| N_{2,0} + k_2 C_{eq}^{1/2} \right|\right)^2 C_{eq} y^*}{\left(\tau_0 + k_1 C_{eq}^{1/2}\right)\gamma_{st}}\,, \tag{4.30}$$

$$k = \bar{k}\left(\frac{\tau_0 \left| N_{2,0} + k_2 C_{eq}^{1/2} \right|}{\gamma_{st} y^*}\right)^{1/2}. \tag{4.31}$$

With these definitions, Equation 4.27 is

$$\bar{s} = \frac{1}{6}\bar{k}^2(3 - 2\bar{k}^2)\,. \tag{4.32}$$

Figure 4.2 is a plot of dimensionless $\bar{s}$ versus $\bar{k}$.

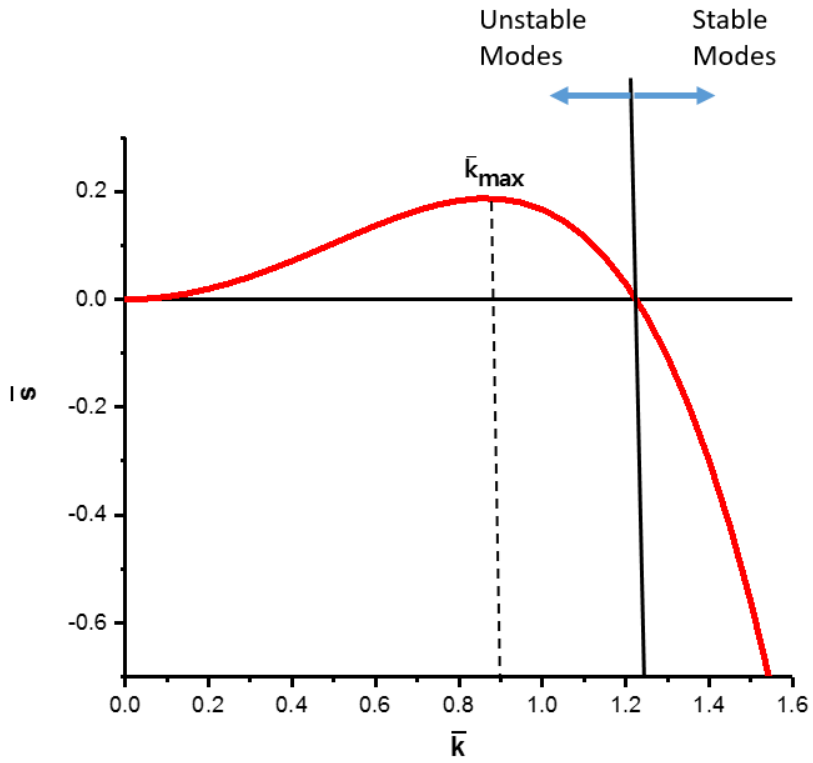

Figure 4.2: $\bar{s}$ versus $\bar{k}$ is plotted. k_{max} is depicted along with the stable and unstable wavenumber ranges.

Fig. 4.2 shows how the values of $\bar{s}$ transition from stable to unstable according to the criterion laid out in Equation 4.32. Lower values of $\bar{k}$ lead to instability while the higher values are increasingly stable. This is due to the stabilization by capillary forces embodied in the negative fourth order term in Equation 4.32. The most unstable mode will be the one that is experimentally realized, meaning that the instability that develops will have the wave number of the fastest growing mode, given by Equation 4.29. To give the reader a

sense of the size scales that would be observed in experiments, Table 4.1 provides model predictions of what the expected wavelengths of instabilities would be in actual materials.

Table 4.1: Parameters are provided for an inclined plane at angle of 45^0 and a density of 1000 kg/m^3. The yield stress is increased from the top row to the bottom and the overall layer thickness, d, is adjusted such that the yield point, y^*, is always equal to 1 mm. The predicted wavelength is given in the right most column in cm. $N_{2,0}$ is set to be 0.09, k_1 is chosen to be 0.2 Pa s$^{0.5}$, k_2 is chosen to be 0.00411 Pa s$^{0.5}$, and γ_{st} is set to be 0.05 N/m.

d (mm)	τ_0 (Pa)	y^* (mm)	q_0 cm^2/s	C_{eq} (1/s)	k_{max} (1/cm)	wavelength (cm)
1.12	1	1.00	4.35	0.870	0.368	17.1
1.6	5	1.00	4.35	0.870	0.822	7.6
2.12	10	1.00	4.35	0.870	1.16	5.4

Table 4.1 shows that the model predicts a decreasing wavelength for an increasing yield stress. It also shows that the model predicts values that are in the expected order of magnitude for the wavelengths that might be seen in experiment.

4.4 Conclusions

A theoretical stability analysis of the gravity driven flow of a visco-plastic liquid down an inclined plane is performed. The material has yield stress, shear-thinning viscous behavior, and exhibits a second normal stress difference. These special characteristics give the material unique and interesting characteristics.

Linear perturbation analysis shows that a wave perturbation that is transverse to the direction of flow has both stable and unstable modes. Stability is determined by a competition between surface tension forces and second normal stresses. Higher second normal stresses as compared to surface tension forces lead to unstable modes because the

stress acts to make perturbations more pronounced. However, high surface tension and low second normal stress difference conditions lead to stability because the surface tension forces act to reduce surface curvature, thus eliminating the waves. The stable waves are found at high wave numbers (high frequency) because these have the strongest curvature. This means that greater stability of the flow can be achieved if the second normal stress differences can be reduced.

The fastest growing mode and the range of unstable wavenumbers was also found to depend on the ratio of second normal stresses to surface tension. In practice, the disturbance with the fastest growing mode will be the one visible experimentally. The higher the ratio is, the shorter the wavelength of the instability will be. It was also found that a wider range of wavenumbers are unstable when this ratio is high. This is seen in the equation given for k_{max}. Stability also decreases when the value of y^* goes up. This means that the larger the liquid region of the fluid is, the larger the range of unstable modes will be.

Chapter 5: Stability of a Power-Law Fluid in a Forward Roll Coating Process

5.1 Introduction

Roll-to-roll coating is a common industrial process for applying coatings and thin films to surfaces. Roll-to-roll coating has a wide variety of industrial applications including production of photo-voltaics [Krebs, F.C. (2009, 2009); Thrane et al. (2012)], paint application [Cohu, O. & Magin, A. (1995); Varela Lopez, F. & Rosen, M. (2002)], and optical coatings[Ting, C.J. et al. (2008); Nogi, M. et al. (2009)]. Roll-to-roll coating processes carry some great advantages. The first is that they allow for fast and continuous coating of substrates. The second is that they create uniform coatings, which is particularly important for optical film and photovoltaic applications.

A common problem in roll coating is the so-called "ribbing instability". This instability is characterized by film thickness striations forming along the axial length of the rollers. Stability of roll-to-roll coating process has been studied extensively for Newtonian fluids experimentally [Mill, C.C. & South, G.R. (1967); Pitts, E. & Greiller, J. (1961); Greener et al. (1980)], computationally[Carvalho, M.S., & Scriven, L.E. (1999); Coyle, D.J. et al. (1990); Chien, C.H. & Jang, J. Y. (2007)], and theoretically[Coyle, D.J. et al. (1986); Savage, M.D. (1984); Carvalho, M.S. & Scriven, L.E. (1997)]. The earliest experiments found that the instability appears only when the capillary number (Ca) is at or above a particular critical value. The computational works solve the flow field and pressure equations using the finite element method and then apply a numerical linear perturbation analysis to the flow to obtain stable and unstable capillary numbers. The theoretical work,

in particular the work of Savage [Savage, M.S. (1984)], primarily focuses on applying linear perturbation analysis to the problem to determine where the critical capillary number lies.

Experimental [Cohu, O. & Magin, A. (1995); Varela Lopez, F. & Rosen, M. (2002); Vareala Lopez et al. (1999); Kang, Y.T. et al. (1991)] and computational [Coyle, D.J. et al. (1987); Zevallos, G.A. et al. (2005)] analyses of the ribbing instability in non-Newtonian fluids can also be found in the literature. However, there are no analytical analyses of ribbing in non-Newtonian forward roll coating. This work seeks to take the analysis done by Savage[Savage, M.S. (1984)] on Newtonian fluids and expand it to power-law fluids to examine the effect of material properties on processing stability.

5.2 Analytical Model of Roll-to-roll Coating Process

5.2.1 Base Case Problem Set Up

We consider lubrication flow of a power-law fluid between two rotating cylinders set up in a forward coating configuration as seen in Fig. 5.1.

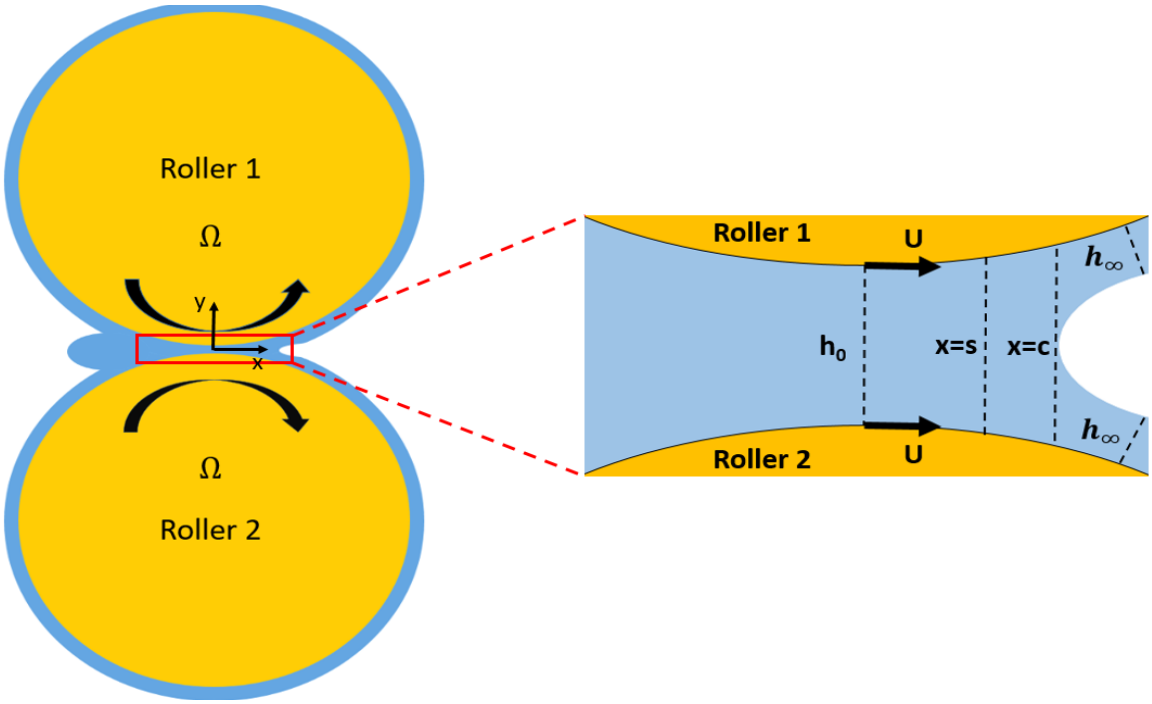

Figure 5.1: a.) The full two roller system is shown on the right with each roller having angular velocity **Ω**. The right side shows a blown up image of the region of interest. The minimum gap distance is h_0 , the stagnation point is shown at $x=s$, the location of the film meniscus is shown as $x=c$, and the final film thickness is given as h_∞.

Fig. 5.1 shows the region of interest in the blown up section of the figure. In this region, the standard lubrication approximation assumptions apply. The distance between rollers is given by:

$$h(x) = h_0 + \frac{x^2}{R} \quad , \tag{5.1}$$

where h_0 is the minimum gap length, $h(x)$ is the gap length at x, and R is the radius of one of the rollers. The lubrication approximation gives Equation 5.2 as the governing equation in gap

$$\frac{\partial P_0}{\partial \mathrm{x}} = \frac{\partial \tau_{\mathrm{xy}}}{\partial \mathrm{y}}. \tag{5.2}$$

In the case of a Herschel-Bulkley fluid, a solid unyielded core would be present in the center of the rollers with yielded fluid behaving according to a power-law relationship. In the lubrication limit, it is not possible to satisfy the pressure boundary conditions and maintain a solid core. Thus, power-law fluid behavior is used in this study as a limiting behavior to understand the flows of shear thinning materials. Under these assumptions, the lubrication equation becomes

$$\frac{\partial P_0}{\partial x} = \frac{\partial}{\partial y}\left[k\left(\frac{du_0}{dy} \right)^n \right], \tag{5.3}$$

with boundary conditions at

$$u_0(x, \frac{h(x)}{2}) = U, \tag{5.4}$$

$$\frac{du_0}{dy}|_{y=0} = 0, \tag{5.5}$$

$$u_0(s, 0) = 0, \tag{5.6}$$

and additional pressure boundary conditions:

$$P_0(-\infty) = 0, \tag{5.7}$$

$$P_0(s) = -T / r \approx -T / \left(\frac{h(s)}{2} - h_\infty \right), \tag{5.8}$$

where u_0 is the base case velocity profile in the x direction, P_0 is the base case pressure, k is a material parameter, n is power-law index of the fluid, U is the tangential roller speed,

T is the surface tension, r is the radius of curvature of the meniscus which is approximated, and s is x position of the stagnation point which is where the fluid velocity reaches 0 between the two rollers. The following non-dimensionalization is then used

$$Uu_0^* = u_0\,,\ h_0 y^* = y\ ,\ h_0 x^* = x\,,\ P_c P_0^* = P_0\ ,$$

(5.9)

$$P_c = \frac{kU^n}{h_0^n}\ , Ca = \frac{kU^n}{h_0^{n-1}T}\,,\ h^*(x) = 1 + ax^2\,,\ a = \frac{h_0}{R}$$

Since the dimensional variables will not be used again, the *'s will be dropped going forward.

5.2.2 Perturbation Problem Set-up

Once the base case velocity profile is known, a perturbation is applied to the position of the stagnation point such that it varies along the axis of the rollers. This perturbation is of the form $s_{new} = s + \varepsilon \sin(\omega z)$, where s_{new} is the perturbed position of the stagnation point, ε is a small parameter, and ω is the frequency of the perturbation. This results in perturbations of the form

$$\boldsymbol{u} = u_0(x, y)\boldsymbol{e}_x + \boldsymbol{u}'\,, \tag{5.10}$$

$$P = P_0 + P' \quad , \tag{5.11}$$

$$\boldsymbol{\tau} = \boldsymbol{\tau_0} + \boldsymbol{\tau}'\,, \tag{5.12}$$

where $\boldsymbol{\tau}'$ is the perturbed stress tensor, $\boldsymbol{\tau_0}$ is the base case stress tensor, $\boldsymbol{\tau}$ is the total stress tensor, P is the total pressure field, P' is the perturbed pressure field, $\boldsymbol{u}$ is the total velocity

vector field, $\boldsymbol{u}'$ is the perturbed velocity vector field, and $\boldsymbol{e}_x$ is the unit vector in the x direction. These are then plugged into the lubrication equations. This results in the following perturbation equations

$$\frac{\partial \tau'_{xy}}{\partial y} = \frac{\partial}{\partial y}\left[\left|\frac{du_0}{dy}\right|^{n-1}\frac{du'_x}{dy}\right] = \frac{\partial P'}{\partial x}, \tag{5.13}$$

$$\frac{\partial \tau'_{zy}}{\partial y} = \frac{\partial}{\partial y}\left[\left|\frac{du_0}{dy}\right|^{n-1}\frac{du'_z}{dy}\right] = \frac{\partial P'}{\partial z}, \tag{5.14}$$

$$\frac{\partial u'_x}{\partial x} + \frac{\partial u'_y}{\partial y} + \frac{\partial u'_z}{\partial z} = 0 \ , \tag{5.15}$$

where τ'_{xy} and τ'_{zy} are the perturbed stress tensor components relevant to this 2-D lubrication problem, u'_x is the perturbed x velocity, u'_y is the perturbed y velocity, and u'_z is the perturbed z velocity. Equation 5.13 is the lubrication equation in the x-direction, Equation 5.14 is the lubrication equation in the z-direction, and Equation 5.15 is the perturbed continuity equation. The following perturbed boundary conditions are then arrived at

$$\frac{du'_x}{dy}(0) = 0 \ , \tag{5.16}$$

$$u'_x\left(\frac{h(x)}{2}\right) = 0 \ , \tag{5.17}$$

$$\frac{du'_z}{dy}(0) = 0 \ , \tag{5.18}$$

$$u_z'\left(\frac{h(x)}{2}\right)=0\ , \tag{5.19}$$

$$P'(-\infty)=0\,, \tag{5.20}$$

$$P'=\left[\frac{2(2n+1)2as}{Ca(n+1)h^2(s)}-\left(\left(\frac{2}{h(s)}\right)^{1/n+1}\left(\frac{n+1}{n}\right)\right)^n+\frac{\omega^2}{Ca}\right]\sin(\omega z)=B\sin(\omega z)\,, \tag{5.21}$$

and, following [Savage, M., 1984], a stability condition

$$\frac{dP'}{dx}|_{x=s}=2^{n+1}h^{-(n+2)}(s)2as\left[\left(\frac{n+1}{2n+1}\right)^{n-1}\left(\frac{2n+1}{n}\right)-(n+1)\left(\frac{n+1}{n}\right)^n\right]\sin(\omega z)\,, \tag{5.22}$$

where ω is the wave number of the disturbance and B is a variable used for shorthand to represent the lengthy part of Equation 5.15's LHS. Equations 5.16 and 5.18 are symmetry boundary conditions on u_x' and u_z', respectively. Equations 5.17 and 5.19 are no slip conditions. Equation 5.20 is the perturbed pressure boundary condition far back into the fluid. Equation 5.18 is the perturbed pressure condition from Equation 5.8. Equation 5.22 is the perturbed pressure gradient condition at the stagnation point. This condition is the minimum required pressure gradient to maintain stability.

5.3 Results and Discussion

Initially, the base unidirectional flow must be computed. The base case flow is determined by two integrations and some algebraic manipulation of Equation 5.3 to obtain

$$u_0(x,y)=\mathrm{sgn}\left(\frac{dP_0}{dx}\right)\left(\frac{dP_0}{dx}\right)^{1/n}\frac{n}{n+1}\left(y^{1/n+1}-\left(\frac{h(x)}{2}\right)^{1/n+1}\right)+1\,. \tag{5.23}$$

The *sgn* operator is used to preserve the sign of the velocity and pressure gradients since the value of n can result in strictly positive numbers for select values of n. This velocity profile can then be integrated to get the overall flowrate. This gives the mass balance

$$\int_0^{\frac{h(x)}{2}} u_0(x,y)dy = \mathrm{sgn}\left(\frac{dP_0}{dx}\right)\left(\frac{dP_0}{dx}\right)^{1/n}\frac{n}{n+1}\left(\frac{-n-1}{2n+1}\right)\left(\frac{h(x)}{2}\right)^{(2n+1)/n} + \frac{h(x)}{2} = h_\infty . \quad (5.24)$$

The base case pressure gradient can then be obtained as

$$\frac{dP_0}{dx} = \left\|\left[\left(\frac{h(x)}{2}-h_\infty\right)\left(\frac{2}{h(x)}\right)^{\frac{2n+1}{n}}\left(\frac{2n+1}{n}\right)\right]\right\|^n \mathrm{sgn}\left(\frac{h(x)}{2}-h_\infty\right) . \quad (5.25)$$

Then the stagnation condition (Equation 5.6) is applied to determine the pressure gradient at the stagnation point, (x=s, y=0). Thus the requirement at the stagnation point for the pressure gradient is

$$\frac{dP_0}{dx}|_{x=s} = \left\|\left[\left(\frac{2}{h(s)}\right)^{\frac{1}{n}+1}\left(\frac{n+1}{n}\right)\right]\right\|^n \mathrm{sgn}\left(\frac{dP_0}{dx}|_{x=s}\right). \quad (5.26)$$

Equation 5.9 is evaluated and set equal to Equation 5.23 to determine h_∞, which is given by

$$h_\infty = \frac{h(s)}{2}\left(\frac{n}{2n+1}\right). \quad (5.27)$$

The final part of the base case problem is to then solve for the value of s and the pressure profile. The pressure boundary condition at the stagnation point is given by

$$P_0(s) = -\frac{2n+1}{Ca(n+1)\left(\frac{h(s)}{2}\right)} \quad . \tag{5.28}$$

The pressure differential equation is solved numerically to find the value of *s*. This completes the solution of the base problem. The pressure profile and velocity profiles can now be determined. Fig. 5.2 shows a plot of the pressure profile for different gap to roller radius ratios, *a*. Fig. 5.3 shows how the pressure profile changes with different values of the power law index n.

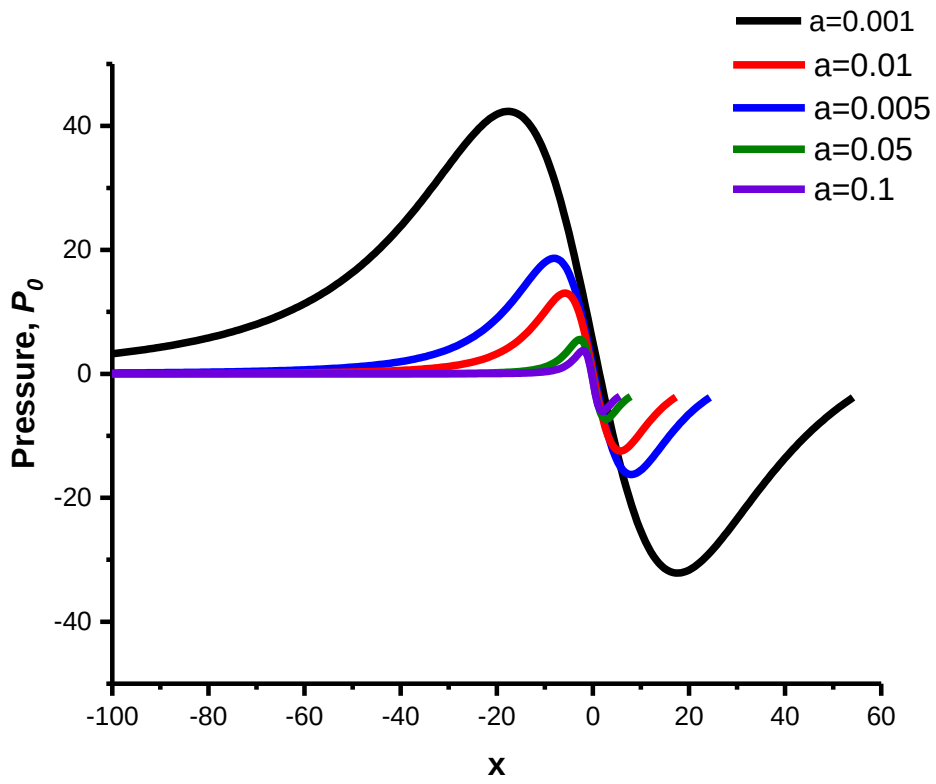

Figure 5.2: Pressure is plotted as a function of x for a Newtonian fluid (n=1). Since an infinite bank of material is assumed as $x \to -\infty$, the pressure becomes 0 as $x \to -\infty$. As the minimum gap length a decreases the pressure change increases.

As the fluid approaches the gap, its pressure rises until it reaches a maximum and then it falls as the pressure drop assists the shear from the rollers in pushing the fluid through the gap to the other side where the pressure reaches a minimum and then rises again to meet the surface tension condition imposed at the fluid meniscus. Similar pressure plots can be made holding a constant and changing the value of the power-law index, n. Fig. 5.3 shows how the pressure field changes as the fluid becomes more and more shear-thinning (decreasing n).

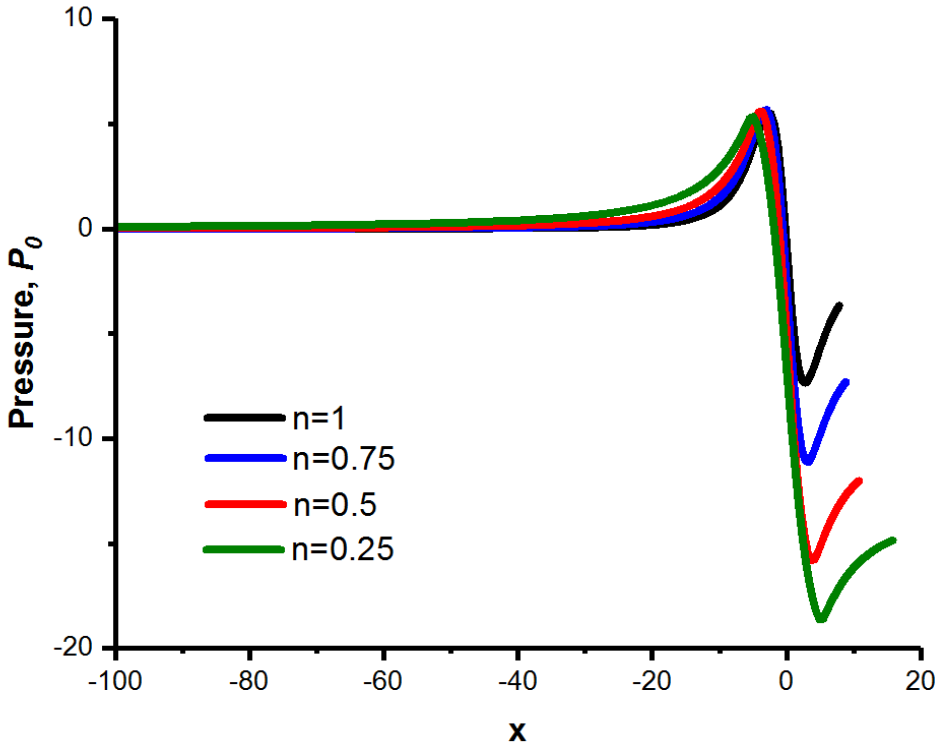

Figure 5.3: Pressure curves are plotted as functions of x for various values of n, while the value of a is fixed at 0.05.

The general shape of the curves is the same as what is observed in Fig. 5.2. The primary difference is that the maximum pressure values decrease just slightly with n, while the minimums drop substantially with n. This is likely due to the fact that the capillary number decreases with decreasing n.

Velocity plots have also been made that show how the fluid's motion responds to these pressure changes. Fig. 5.4 depicts the velocity field for two different power-law indices at three different x locations.

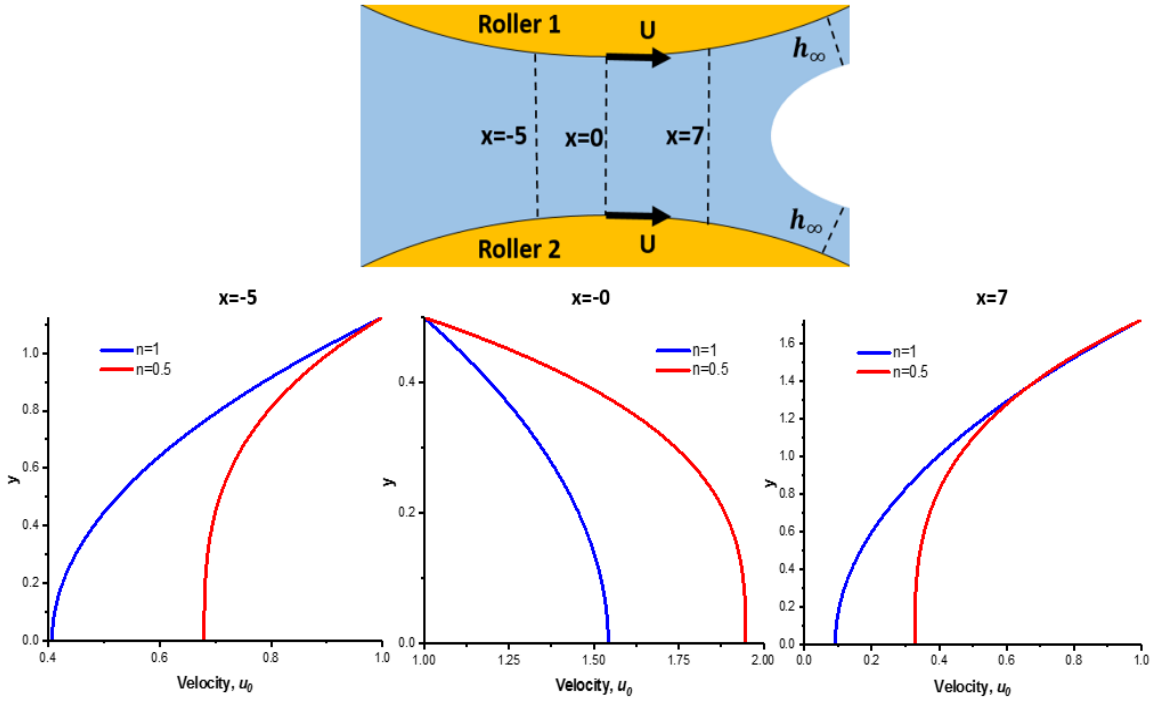

Figure 5.4: Velocity profiles for different x locations. Velocities are plotted such that y=0 corresponds to the line of symmetry between the rollers and x=0 corresponds to the nip (location of the smallest gap length). From left to right, velocities are plotted at a location before the nip (x=-5), at the nip (x=0), and near the stagnation point (x=7).The location of the stagnation point in this system is x=7.8. The blue line shows the velocity field of a Newtonian fluid while the red shows a power-law fluid with n=0.5.

The left plot of Fig. 5.4 shows how both fluids how their slowest velocities at the line of symmetry as the pressure builds as the fluid approaches the nip. The middle plot shows how the pressure gradient being negative forces the fluids through the nip. Finally, the fluids slow down again near the line of symmetry as they approach the stagnation point where the center velocity will reach a value of 0.

The base case flow is found, next the perturbation equations must be solved in order to analyze the stability of this roll-to-roll set up to the ribbing instability. The standard

sinusoidal perturbation is introduced to the position of the stagnation point. The resulting pressure from this is given by

$$P' = \varepsilon \hat{P}(x)\sin(\omega z)\,. \tag{5.29}$$

Equations 5.13 and 5.14 are then solved with their respective boundary conditions to yield the following expressions for the perturbed velocities

$$u_x' = \left(\frac{dP_0}{dx}\right)^{\frac{1-n}{n}} \frac{d\hat{P}}{dx}\left(\frac{n}{n+1}\right)\left(y^{\frac{n+1}{n}} - \left(\frac{h(x)}{2}\right)^{\frac{n+1}{n}}\right)\mathrm{sgn}\left(\frac{dP_0}{dx}\right)\sin(\omega z)\,, \tag{5.30}$$

$$u_z' = \omega\left(\frac{dP_0}{dx}\right)^{\frac{1-n}{n}} \hat{P}\left(\frac{n}{n+1}\right)\left(y^{\frac{n+1}{n}} - \left(\frac{h(x)}{2}\right)^{\frac{n+1}{n}}\right)\mathrm{sgn}\left(\frac{dP_0}{dx}\right)\cos(\omega z)\,. \tag{5.31}$$

When these perturbation equations are combined with the continuity equation, the following relationship for the perturbed pressure can be derived by integrating over y

$$\frac{d^2\hat{P}}{dx^2} + \frac{\frac{dh}{dx}\left(\left(\frac{n+2}{n}\right)h(x) - h(s)\right)(2n+1)}{h(x)\left(\left(\frac{2n+1}{n}\right)h(x) - h(s)\right)}\frac{d\hat{P}}{dx} - \omega^2\hat{P} = 0\,, \tag{5.32}$$

with boundary conditions

$$\hat{P}(-\infty) = 0\,, \tag{5.33}$$

$$\hat{P}(s) = \left[\frac{2(2n+1)2as}{Ca(n+1)h^2(s)} - \left(\left(\frac{2}{h(s)}\right)^{1/n+1}\left(\frac{n+1}{n}\right)\right)^n + \frac{\omega^2}{Ca}\right] = B\,. \tag{5.34}$$

Equation 5.32 has variable coefficients that have two singularities in the domain and would need to be solved numerically. However, since the stability is determined by the behavior

of the pressure gradient near the stagnation point, we can obtain an approximate analytical solution to the pressure boundary value problem by evaluating the first order derivative's coefficient at $x=s$ and then solving the resulting constant coefficient ODE. The approximate solution of Equation 5.32 is given by

$$\hat{P} = Be^{\left(-A+\sqrt{A^2+4\omega^2}\right)(x-s)}, \tag{5.35}$$

$$A = \frac{4as\left(2n+1\right)}{(n+1)h(s)}. \tag{5.36}$$

Finally, the stability condition can be applied. The stability condition is the perturbed pressure gradient condition

$$\frac{d\hat{P}}{dx}|_{x=s} = 2^{n+1}h^{-(n+2)}(s)2as\left[\left(\frac{n+1}{2n+1}\right)^{n-1}\left(\frac{2n+1}{n}\right)-(n+1)\left(\frac{n+1}{n}\right)^{n}\right]. \tag{5.37}$$

Equation 5.37 gives the minimum requirement on the pressure gradient at the stagnation point for stability. If the pressure gradient falls below this, the stagnation point will not be stable and the instability will occur. The results of this stability analysis are shown in Fig. 5.5.

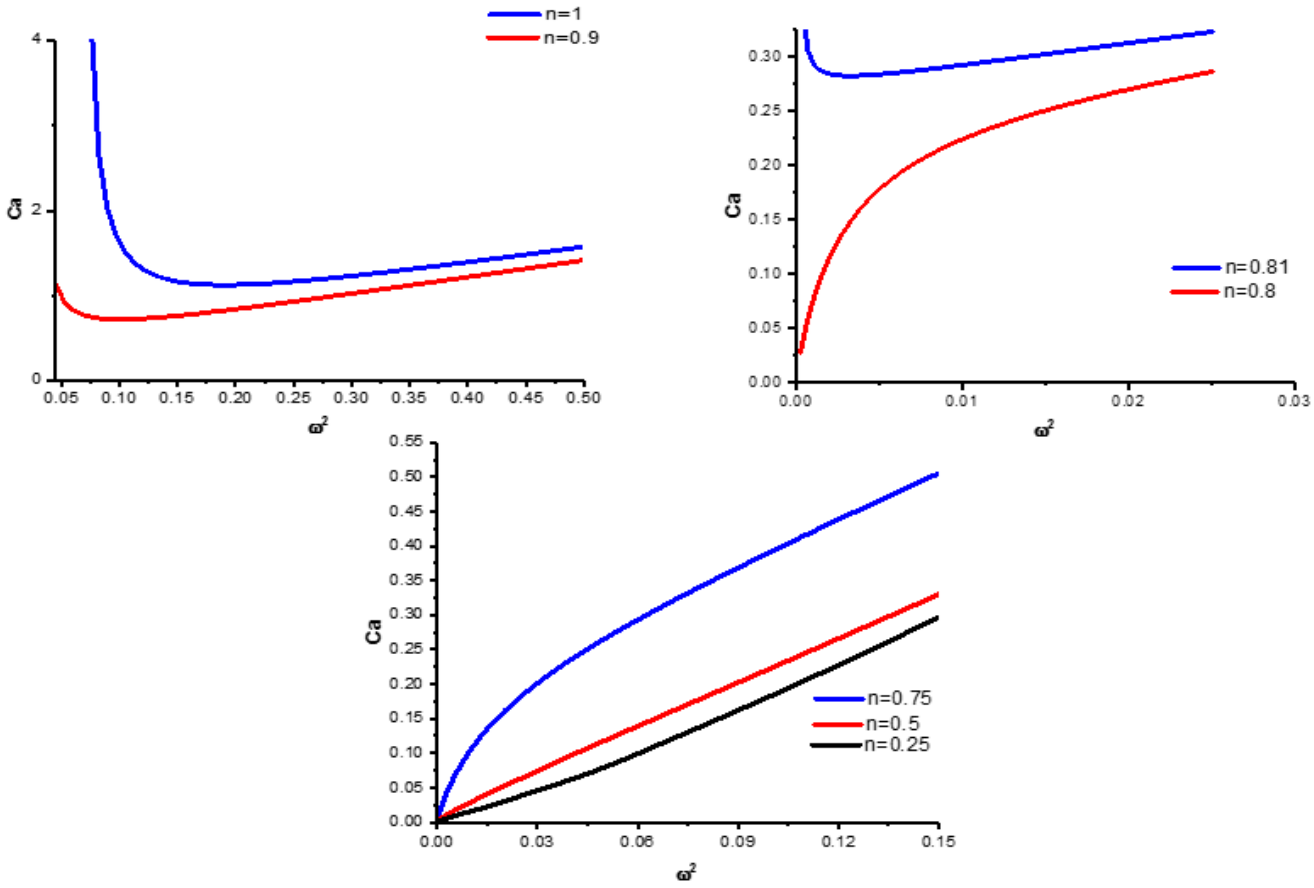

Figure 5.5: Minimum stable capillary numbers are plotted as a function of disturbance frequency squared for a variety of *n* values between 1 and 0.25. The general shape of the graph is seen to change in the top right plot as *n* changes from 0.81 to 0.8.

Results plotted in Fig. 5.5 show a qualitative change in the shape of the neutral stability curve as n changes from 0.81 to 0.8. Power law indices above 0.8 have a minimum capillary number above which some modes become unstable, but below which are stable. Once *n*=0.8 or less, however, there is no longer a minimum stable capillary number and all capillary numbers are unstable to some part of the wavenumber spectrum. This occurs because the stability condition (5.37) requires a pressure gradient that is negative for

stability for values above 0.8, but at n=0.8 and below the stability condition requires a positive pressure gradient. This positive pressure gradient ensures that for any capillary number, when n=0.8 or below, some perturbation wave modes will be unstable.

A comparison that can be made with data that was obtained with gels in Dr. Cloitre's rheology lab. Two rollers are used to mix gels with n=0.5 and a in the range of 0.005 to 0.06. When the experiment beings, a mass of paste is placed between the rollers as they rotate. The pastes spreads out along the axis of the roller until it reaches a steady state length. Pictures were then taken of the apparatus. These pictures show periodically spaced ridges along the axial length of the rollers. Three different masses of paste were experimented with: 6 grams, 12 grams and 18 grams and different gap sizes, $h_{0,}$ were used. The spread length and the number of ridges were measured in each case. A photo of one of the experiments is shown in Fig. 5.6. The data from these experiments is then shown in Fig 5.7.

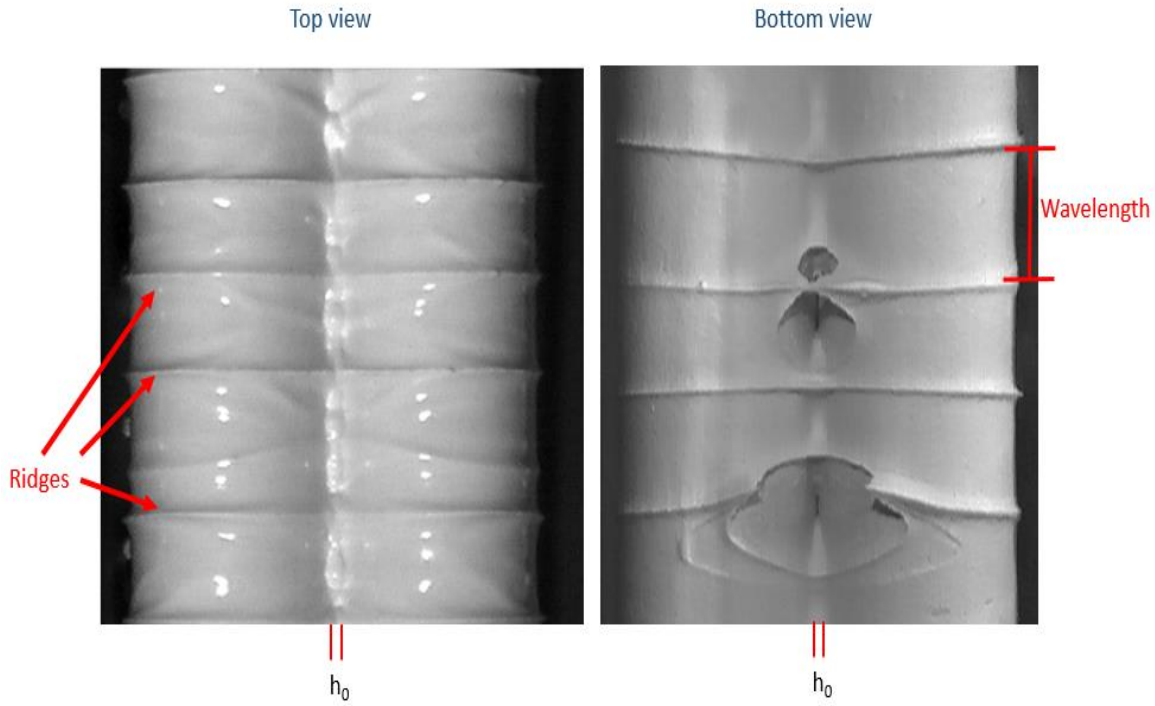

Figure 5.6: A picture of the experimental apparatus for roll-to-roll paste coating is shown. The instability is seen as the ridges that form along the axis of the rollers. The left picture shows a view of the rollers such that the paste in the gap is flowing into the page while the image on the right shows it on the other side where paste is flowing out of the page.

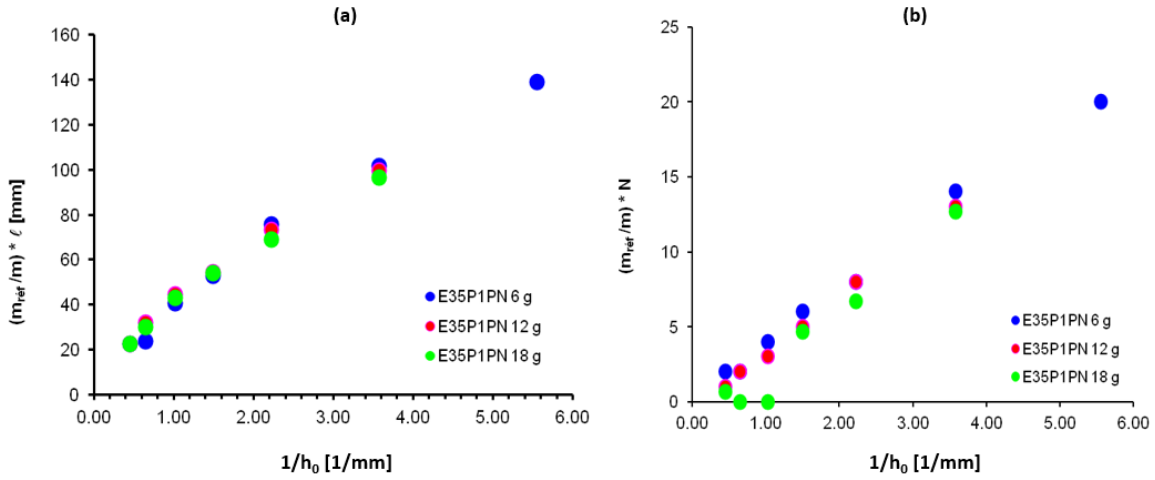

Figure 5.7: Graph (a) plots the spread length, ℓ, weighted by the ratio of a m_{ref}/m which is the ratio of a references mass, chosen to be 12 grams here, and the sample mass against the reciprocal of the gap length, h_0, in mm for three different masses of paste: 6 g in blue, 12 g in red, and 18 g in green. Graph (b) plots the number of ridges, N, weighted by the ratio m_{ref}/m versus the reciprocal of the gap length, h_0.

Fig. 5.7 shows that both plots, (a) and (b), show a strong linear trend and differences between masses are seen to minor. For each gap size, the average weighted spread length (averaged between the masses) can be divided by the average weighted number of ridges to obtain a wavelength and then a wave number. Fig. 5.8 has the comparison of these experimentally obtained wave numbers with the theoretical model derived.

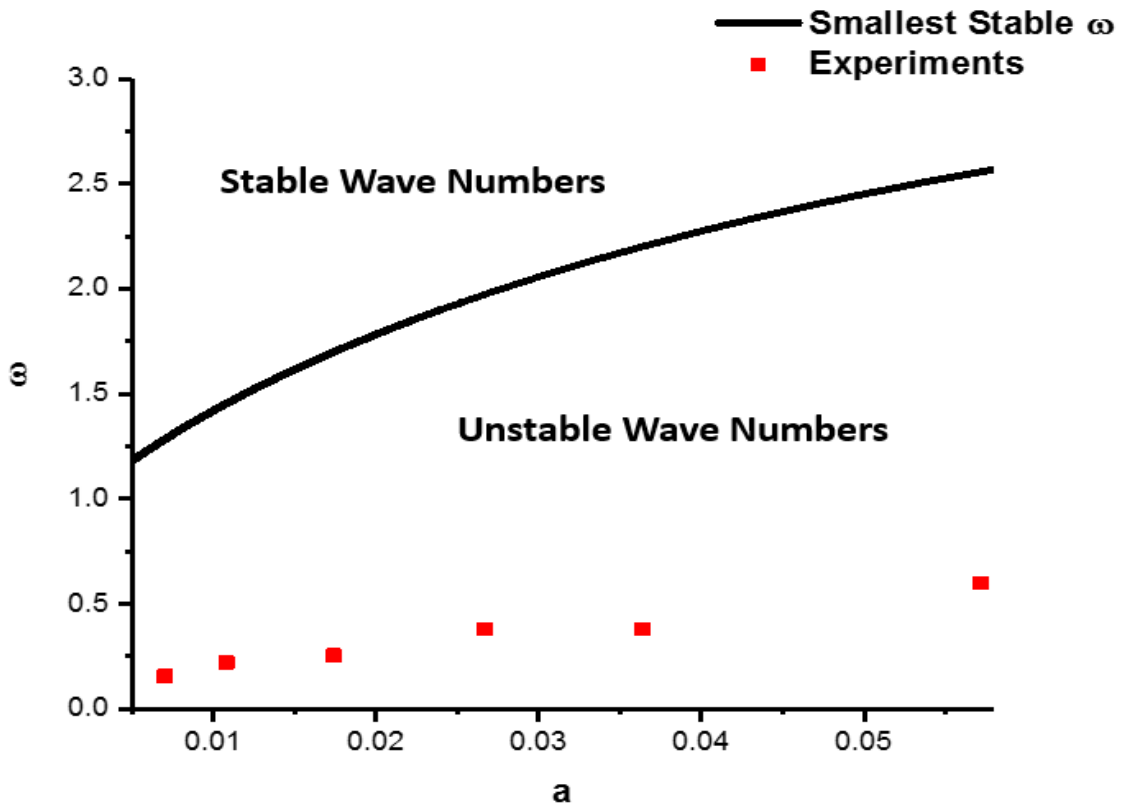

Figure 5.8: The black line plotted represents the minimum stable ω. The experimental data points in red were taken from Dr. Cloitre's experiments with gels. The unstable waves exhibit wave numbers in the expected range.

The results from the experiments always showed some instability in all of the conditions that were experimented on. Fig. 5.6 shows that the wavenumbers of these observed instabilities lie in the expected range. The results of this theoretical study suggest that the reason this instability is always present is that, for power-law index values below 0.81, there are always some wavenumbers that are unstable.

5.4 Conclusions

A theoretical stability analysis of forward roll coating of a power-law fluid is performed. This stability analysis seeks to use this power law fluid to approximate the behavior of a soft particle paste which has yield stress, shear-thinning viscous behavior, and second normal stress-difference. This is a good approximation because there should not be any solid portions in the flow field between the rollers because the solid piece would need to be still, but this does not allow the flow to meet the surface tension boundary condition at the meniscus. The second normal stress differences are not required to explain the occurrence of these instabilities that are present for all tested conditions.

A perturbation analysis originally used by Savage is expanded to be used on power-law fluids so as to explore the stability of these flows. The perturbation analysis presented here finds that for materials with a power-law index below a critical value, n=0.81, the stability criterion changes fundamentally and the flow becomes unstable at every capillary number for some wave numbers. Physically, this suggests that as n decreases the perturbed base case pressure gradient becomes higher than the second derivative of the base case pressure (which is required for flow continuity). Once this occurs, elements of the fluid perturbed beyond the stagnation line experience a force that pushes the fluid forward to feed the ribs. The transition that occurs when n=0.81 comes about because the perturbed pressure gradient switches from being negative, at n=0.81, to being positive at n=0.8. This guarantees that the perturbed pressure gradient condition, when the gradient is positive, will always have some wavenumbers that will be unstable.

These findings are reinforced by experimental results obtained by the Cloitre lab. The experimental findings suggest that the instability is always present for all the conditions tested. This result is supported by the model because the power law index in the fluid is n=0.5 and this is well below the transition found in this work, n=0.81, where some wave numbers are always seen to be unstable. The unstable wave numbers found in the experiments are below the maximum predicted stable wave numbers.

Chapter 6: Summary, Conclusions, and Future Work

6.1 Summary and Conclusions

This work has focused on interfacial dynamics in different processing methods for elastic fluids. The first process is a polymer co-extrusion as explained in chapters 2 and 3. The results from Chapters 2 and 3 identify methods for improvement of a multilayer co-extrusion process, which Chapter 2 focusing on improvement of the feedblock and Chapter 3 focusing on improvement of the multiplier dies. The second half of this work focuses on processing of Herschel-Bulkley fluids with second normal stress differences. Chapter 4 addresses the stability of flow of this material down an inclined plane. Chapter 5 then covers flow of this type of material in a forward roll coating process.

Work in Chapter 2 features simulations of a multilayer co-extrusion feedblock. These feedblock simulations explore two different ideas for reducing interfacial deformation between the layers in the feedblock. The first of these ideas is to reduce the wall friction to reduce the shear on the material. This is done to reduce the second normal stress differences, which are responsible for the interface deformation. The second of these ideas is to increase the initial number of layers. This is done to distribute the second normal stress differences throughout the channel, resulting in less deformation per layer. Both of these methods were observed to reduce the amount of deformation in the layered structures in the process.

Chapter 3 goes on to cover how multiplier dies can be redesigned to improve the co-extrusion process. The first topic explored with simulations is how to reduce pressure drop across the die by changing the die design. The die design is adjusted so that the die

cross-section is kept constant, which is different from the original die design that contracts first and then expands. This is found to reduce the pressure drop through a multiplier die by 40% in all cases simulated. The second topic explored is how to re-design the multiplier die to improve the interface shape. This die design uses a cross-section that has a very high aspect ratio to reduce the effects of side wall shear on the multi-layer flow, thus localizing interface distortion only to small portions near the side walls. Simulations shown in this chapter demonstrate that this die design is very effective at reducing interface deformation in the channel and localizing deformation near the side walls. The chapter concludes by showing photos of experimental results obtained by experimental collaborators. These photos show that the proposed improvements from Chapters 2 and 3 can improve the quality of the layered structures obtained.

Chapter 4 studies the stability of a Herschel-Bulkley fluid with a second normal stress difference down an inclined plane. The standard linear stability analysis is applied to the problem with the perturbation being applied perpendicular to the primary direction of flow. Stability is studied for a range of wave numbers and stable and unstable ranges were determined. The fastest growing wave mode is also calculated for the flow. It is found that the instability comes about from a competition between destabilizing second normal stress differences and stabilizing surface tension forces. It is also found that stability depends heavily on the values of the yield stress, with instability frequency increasing with increasing yield stress. Results also show that flows with thicknesses on the order of

millimeters tend to have the strongest destabilizing disturbance wavelengths on the order of centimeters.

Chapter 5 then examines the stability of flow of the same Herschel-Bulkley fluid in Chapter 4 in a forward roll configuration to ribbing. The method of Savage is employed to study the stability of these flows. This analytical method is extended to be used for power-law fluids. Pressure and flow fields are determined in the base case for a variety of gap sizes and power law indices. The stability of the flow is explored for various power law indices and it is found that for values below n=0.8, the flow is always unstable to some wave modes. This result matches up with experimental findings from Dr. Cloitre's lab. His experiments show that all configurations are unstable for the materials he was using, which is partial confirmation of this analytical result. The conditions in his experiments and the measured wavelengths all fall into a region predicted to be unstable by the model, further validating the model.

6.2 Recommended Future Work

One area that would be very interesting for future work is co-extrusion of polymers with very low viscosities such as liquid crystal polymers, with other highly viscous polymers such as PMMA. This was something that our experimental collaborators mentioned having great difficulty with in their co-extruder. Computational studies around this would be very interesting from an applications point of view because it could potentially allow the creation of multi-layered materials with high viscosity/high elasticity materials and low viscosity materials such as liquid crystal polymers. It would also be

interesting from a computational point of view because the deformation in these systems would likely be very strong and it may be challenging to simulate. It would be particularly interesting to try simulating this using the CDFEM method.

Another area that would be interesting for future work would be forward roll-to-roll experiments on the types of Herschel-Bulkley fluids studied in Chapters 4 and 5. There are currently few experiments that include material properties, gap sizes, roller diameters, roller lengths, and rotational speed settings at which the instability occurs. Experiments with pictures that report all of these properties would be very helpful for further testing of the model presented in Chapter 5 of this work. It would also be interesting to attempt to expand this model to find the fastest growing disturbance mode, which is something that the method proposed by Savage cannot currently do.

References

Allouche, M. H., Millet, S., Botton, V., Henry, D., Hadid, H. B., & Rousset, F. (2015). Stability of a flow down an incline with respect to two-dimensional and three-dimensional disturbances for Newtonian and non-Newtonian fluids. *Physical Review E*, *92*(6), 063010.

Anderson, P. D., Dooley, J., & Meijer, H. E. (2006). Viscoelastic effects in multilayer polymer extrusion. *Applied Rheology*, *16*(4), 198-205.

Armstrong, S. R., Offord, G. T., Paul, D. R., Freeman, B. D., Hiltner, A., & Baer, E. (2014). Co-extruded polymeric films for gas separation membranes. *Journal of Applied Polymer Science*, *131*(2).

Alstrup, J., Jørgensen, M., Medford, A. J., & Krebs, F. C. (2010). Ultra fast and parsimonious materials screening for polymer solar cells using differentially pumped slot-die coating. *ACS Applied Materials & Interfaces*, *2*(10), 2819-2827.

Borzacchiello, D., Leriche, E., Blottiere, B., & Guillet, J. (2014). On the mechanism of viscoelastic encapsulation of fluid layers in polymer co-extrusion. *Journal of Rheology*, *58*(2), 493-512.

Carvalho, M. S., & Scriven, L. E. (1997). Deformable roll coating flows: steady state and linear perturbation analysis. *Journal of Fluid Mechanics*, *339*, 143-172.

Carvalho, M. S., & Scriven, L. E. (1999). Three-dimensional stability analysis of free surface flows: application to forward deformable roll coating. *Journal of Computational Physics*, *151*(2), 534-562.

Chabert, E.: Simulation and Analysis of the Multiphase flow and Stability of Co-Extruded Layered Polymeric Films. Master Thesis, University of Texas at Austin (2011)

Chien, C. H., & Jang, J. Y. (2007). Numerical and experimental studies of thin liquid film flow between two forward-rollers. *Journal of mechanical science and technology*, *21*(11), 1892-1900.

Coyle, D. J., Macosko, C. W., & Scriven, L. E. (1986). Film-splitting flows in forward roll coating. *Journal of Fluid Mechanics*, *171*, 183-207.

Coyle, D. J., Macosko, C. W., & Scriven, L. E. (1990). Stability of symmetric film-splitting between counter-rotating cylinders. *Journal of Fluid Mechanics*, *216*, 437-458.

Cohu, O., & Magnin, A. (1995). Rheometry of paints with regard to roll coating process. *Journal of Rheology*, *39*(4), 767-785.

Debbaut, B., Avalosse, T., Dooley, J., & Hughes, K. (1997). On the development of secondary motions in straight channels induced by the second normal stress difference: experiments and simulations. *Journal of Non-Newtonian Fluid Mechanics*, *69*(2), 255-271.

Denn, M. M. (2008). *Polymer melt processing: foundations in fluid mechanics and heat transfer*. Cambridge University Press.

Dooley, J.: Viscoelastic Flow Effects in Multilayer Polymer Co-extrusion. Ph.D. Thesis, Eindhoven University of Technology (2002)

Dooley, J., Rudolph, L., "Viscous and Elastic Effects in Polymer Co-extrusion", Journal of Plastic Film and Sheeting, **19**, 111-122 (2003)

Dooley, J., "Experimental and Numerical Modeling of the Co-extrusion Process", Proceedings of the Polymer Processing Society 26th Annual Meeting, (2010)

Geise, G. M., Lee, H. S., Miller, D. J., Freeman, B. D., McGrath, J. E., & Paul, D. R. (2010). Water purification by membranes: the role of polymer science. *Journal of Polymer Science Part B: Polymer Physics*, *48*(15), 1685-1718.

German, R. M. (1990). *Powder injection molding* (pp. 124-127). Princeton, NJ: Metal Powder Industries Federation.

Gifford, W. A. (1997). A three-dimensional analysis of co-extrusion. *Polymer Engineering & Science*, *37*(2), 315-320.

Gifford, W. A. (2000). A three-dimensional analysis of co-extrusion in a single manifold flat die. *Polymer Engineering & Science*, *40*(9), 2095-2100.

Greener, J., Sullivan, T., Turner, B., & Middleman, S. (1980). Ribbing instability of a two-roll coater: Newtonian fluids. *Chemical Engineering Communications*, *5*(1-4), 73-83.

Guenette, R., Fortin, M., "A New Mixed Finite-Element Method for Computing Viscoelastic Flows", Journal of Non-Newtonian Fluid Mechanics, **60** 27-52 (1995)

Gupta, A. S. (1967). Stability of a visco-elastic liquid film flowing down an inclined plane. *Journal of fluid mechanics*, *28*(1), 17-28.

Han, C. D., & Shetty, R. (1976). Studies on multilayer film co-extrusion i. the rheology of flat film co-extrusion. *Polymer Engineering & Science*, *16*(10), 697-705.

Harris, P. J., Patz, J., Huntington, B. A., Bonnecaze, R. T., Meltzer, D., & Maia, J. (2014). Improved interfacial surface generator for the co-extrusion of micro-and nanolayered polymers. *Polymer Engineering & Science*, *54*(3), 636-645.

Hatzikiriakos, S. G., & Migler, K. B. (Eds.). (2004). *Polymer processing instabilities: control and understanding*. CRC Press.

Huntington, B. A., Chabert, E., Rahal, S., Patz, J., Silva, J., Harris, P., ... & Bonnecaze, R. T. (2013). Distortion of Interfaces in a Multilayer Polymer Co-extrusion Feedblock. *International Polymer Processing*, *28*(3), 274-280.

Huang, R. (2014). *Multilayer Co-Extrusion and Twin-Screw Compounding of Polymeric Elastomer Systems* (Doctoral dissertation, Case Western Reserve University).

Huang, R., Silva, J., Huntington, B. A., Patz, J., Andrade, R., Harris, P. J., ... & Maia, J. M. (2015). Co-Extrusion Layer Multiplication of Rheologically Mismatched Polymers: A Novel Processing Route. *International Polymer Processing*, *30*(3), 317-330.

Hwang, C. C., Chen, J. L., Wang, J. S., & Lin, J. S. (1994). Linear stability of power law liquid film flows down an inclined plane. *Journal of physics D: applied physics*, *27*(11), 2297.

Jarus, D., Hiltner, A., & Baer, E. (2002). Barrier properties of polypropylene/polyamide blends produced by microlayer co-extrusion. *Polymer*, *43*(8), 2401-2408.

Ji, S., Yin, K., Mackey, M., Brister, A., Ponting, M., & Baer, E. (2013). Polymeric nanolayered gradient refractive index lenses: technology review and introduction of spherical gradient refractive index ball lenses. *Optical Engineering*, *52*(11), 112105-112105.

Kang, Y. T., Lee, K. Y., & Liu, T. J. (1991). The effect of polymer additives on the performance of a two-roll coater. *Journal of applied polymer science*, *43*(6), 1187-1195.

Karagiannis, A., Hrymak, A. N., & Vlachopoulos, J. (1990). Three-dimensional studies on bicomponent extrusion. *Rheologica Acta*, *29*(1), 71-87.

Krebs, F. C. (2009). Polymer solar cell modules prepared using roll-to-roll methods: knife-over-edge coating, slot-die coating and screen printing. *Solar Energy Materials and Solar Cells*, *93*(4), 465-475.

Krebs, F. C. (2009). Roll-to-roll fabrication of monolithic large-area polymer solar cells free from indium-tin-oxide. *Solar Energy Materials and Solar Cells*, *93*(9), 1636-1641.

Krebs, F. C. (2009). All solution roll-to-roll processed polymer solar cells free from indium-tin-oxide and vacuum coating steps. *Organic Electronics*, *10*(5), 761-768.

Larson, R.G., "Chapter 3 Polymers", in The Structure and Rheology of Complex Fluids, Gubbins, K. (Ed.), Oxford University Press, New York, p. 107-188 (1999)

Lee, N. C. (2000). *Understanding blow molding*. Hanser.

Li, H., Tung, K. K., Paul, D. R., & Freeman, B. D. (2011). Effect of film thickness on auto-oxidation in cobalt-catalyzed 1, 4-polybutadiene films. *Polymer*, *52*(13), 2772-2783.

Lott, J., Ryan, C., Valle, B., Johnson, J. R., Schiraldi, D. A., Shan, J., ... & Weder, C. (2011). Two-Photon 3D Optical Data Storage via Aggregate Switching of Excimer-Forming Dyes. *Advanced Materials*, *23*(21), 2425-2429.

Malloggi, F., Andreotti, B., & Clément, E. (2015). Nonlocal effects in sand flows on an inclined plane. *Physical Review E*, *91*(5), 052202.

Mao, G., Andrews, J., Crescimanno, M., Singer, K. D., Baer, E., Hiltner, A., ... & Shakya, B. (2011). Co-extruded mechanically tunable multilayer elastomer laser. *Optical Materials Express*, *1*(1), 108-114.

Michaeli, W. (2003). *Extrusion dies for plastics and rubber: design and engineering computations*. Hanser Verlag.

Mueller, C. D., Nazarenko, S., Ebeling, T., Schuman, T. L., Hiltner, A., & Baer, E. (1997). Novel structures by microlayer co-extrusion—talc-filled PP, PC/SAN, and HDPE/LLDPE. *Polymer Engineering & Science*, *37*(2), 355-362.

Nogi, M., 能木雅也, Yano, H., & 矢野浩之. (2009). Optically transparent nanofiber sheets by deposition of transparent materials: A concept for a roll-to-roll processing. *Applied Physics Letters*, *94*(23), 233117. optical coatings.

Perdikoulias, J., & Tzoganakis, C. (1995). Interfacial instability phenomena in blown film co-extrusion of polyethylene resins. In *TECHNICAL PAPERS OF THE ANNUAL TECHNICAL CONFERENCE-SOCIETY OF PLASTICS ENGINEERS INCORPORATED* (pp. 176-176). SOCIETY OF PLASTICS ENGINEERS INC.

Pitts, E., & Greiller, J. (1961). The flow of thin liquid films between rollers. *Journal of Fluid Mechanics*, *11*(1), 33-50.

Ponting, M., Hiltner, A., & Baer, E. (2010, August). Polymer nanostructures by forced assembly: process, structure, and properties. In *Macromolecular symposia* (Vol. 294, No. 1, p. 19). WILEY-VCH Verlag.

Ponting, M., Burt, T. M., Korley, L. T., Andrews, J., Hiltner, A., & Baer, E. (2010). Gradient multilayer films by forced assembly co-extrusion. *Industrial & Engineering Chemistry Research*, *49*(23), 12111-12118.

Richard, G. L., Ruyer-Quil, C., & Vila, J. P. (2016). A three-equation model for thin films down an inclined plane. *Journal of Fluid Mechanics*, *804*, 162-200.

Rosato, D. V., & Rosato, M. G. (2012). *Injection molding handbook*. Springer Science & Business Media.

Ryan, C., Christenson, C. W., Valle, B., Saini, A., Lott, J., Johnson, J., ... & Shan, J. (2012). Roll-to-Roll Fabrication of Multilayer Films for High Capacity Optical Data Storage. *Advanced Materials*, *24*(38), 5222-5226.

Savage, M. D. (1984). Mathematical model for the onset of ribbing. *AIChE journal*, *30*(6), 999-1002.

Savage, M. D. (1977). Cavitation in lubrication. Part 1. On boundary conditions and cavity—fluid interfaces. *Journal of Fluid Mechanics*, *80*(4), 743-755.

Savage, M. D. (1977). Cavitation in lubrication. Part 2. Analysis of wavy interfaces. *Journal of Fluid Mechanics*, *80*(4), 757-767.

Schrenk, W. J., Shastri, R. K., Roehrs, H. C., & Ayres, R. E. (1996). *U.S. Patent No. 5,540,878*. Washington, DC: U.S. Patent and Trademark Office.

Schroers, J., Pham, Q., Peker, A., Paton, N., & Curtis, R. V. (2007). Blow molding of bulk metallic glass. *Scripta Materialia*, *57*(4), 341-344.

Sunwoo, K. B., Park, S. J., Lee, S. J., Ahn, K. H., & Lee, S. J. (2001). Numerical simulation of three-dimensional viscoelastic flow using the open boundary condition method in co-extrusion process. *Journal of non-newtonian fluid mechanics*, *99*(2), 125-144.

Thrane, L., Jørgensen, T. M., Jørgensen, M., & Krebs, F. C. (2012). Application of optical coherence tomography (OCT) as a 3-dimensional imaging technique for roll-to-roll coated polymer solar cells. *Solar Energy Materials and Solar Cells*, *97*, 181-185.

Ting, C. J., Chang, F. Y., Chen, C. F., & Chou, C. P. (2008). Fabrication of an antireflective polymer optical film with subwavelength structures using a roll-to-roll micro-replication process. *Journal of Micromechanics and Microengineering*, *18*(7), 075001.

Torres, A., Hrymak, A. N., Vlachopoulos, J., Dooley, J., & Hilton, B. T. (1993). Boundary conditions for contacts lines in co-extrusion flows. *Rheologica acta*, *32*(6), 513-525.

Varela López, F., Pauchard, L., Rosen, M., & Rabaud, M. (1999). Threshold of ribbing instability with non-Newtonian fluids. *Advances in Coating and Drying of Thin Films, Shaker, Aachen*, 177-182.

Varela López, F., & Rosen, M. (2002). Rheological effects in roll coating of paints. *Latin American applied research*, *32*(3), 247-252.

Wagner, J. R. (2010). Hand Book of Multilayer flexible packaging technology and applications for food, personal care and over-the counter pharmaceutical industries.

White, J.L., Lee, B.L., "Theory of Interface Distortion in Stratified 2-Phase Flow", Transactions of the Society of Rheology, **19** 457-479 (1997)

Wilson, G. M., & Khomami, B. (1992). An experimental investigation of interfacial instabilities in multilayer flow of viscoelastic fluids: Part I. Incompatible polymer systems. *Journal of non-newtonian fluid mechanics*, *45*(3), 355-384.

Wilson, G. M., & Khomami, B. (1993). An experimental investigation of interfacial instabilities in multilayer flow of viscoelastic fluids. Part II. Elastic and nonlinear effects in incompatible polymer systems. *Journal of Rheology*, *37*(2), 315-339.

Yih, C. S. (1955). Stability of two-dimensional parallel flows for three-dimensional disturbances. *Quarterly of Applied Mathematics*, *12*(4), 434-435.

Yih, C. S. (1965). Stability of a Non-Newtonian Liquid Film Flowing Down an Inclined Plane. *The Physics of Fluids*, *8*(7), 1257-1262.

Yue, P., Zhou, C., Dooley, J., & Feng, J. J. (2008). Elastic encapsulation in bicomponent stratified flow of viscoelastic fluids. *Journal of Rheology*, *52*(4), 1027-1042.